A Closer Look into Slickensides: Deformation On and Under Fault Surfaces

Daniel Ortega-Arroyo & Matej Pec

Department of Earth, Atmospheric, and Planetary Sciences, Massachusetts Institute of Technology, Cambridge, Massachusetts, 02139, USA

Corresponding author: Daniel Ortega-Arroyo (dortega@mit.edu)

Key Points:

- Fault surfaces exhibit a non-Gaussian self-affine roughness with scale-dependent skewness and kurtosis.
- Progressive localization of strain along oriented fabrics give rise to slickenside structures
- Nanoparticulate layers are common on fault rocks regardless of lithology or tectonic setting

Key Words: fault mirror, slickenside, fault surface roughness, principal slip zone, nanograins

Abstract

Accurate descriptions of natural fault surfaces and associated fault rocks are important for understanding fault zone processes and properties. Slickensides--grooved polished surfaces that record displacement and wear along faults-- develop measurable roughness and characteristic microstructures during fault slip. We quantify the roughness of natural slickensides from three different fault surfaces by calculating the surfaces power spectra and height distributions and analyze the microstructures formed above and below the slickensides. Slickenside surfaces exhibit anisotropic self-affine roughness with corresponding mean Hurst exponents in directions parallel-- 0.53±0.07-- and perpendicular --0.6±0.1-- to slip, consistent with reports from other fault surfaces. Additionally, surfaces exhibit non-Gaussian height distributions, with their skewness and kurtosis roughness parameters having noticeable dependence on the scale of observation. Below the surface, microstructural analyses reveal that S-C-C' fabrics develop adjacent to a C-plane-parallel principal slip zone characterized by a sharp decrease in clast size and a thin (≤100 μm) nanoparticulate-rich principal slip surface (PSS). These microstructures are present in most analyzed samples suggesting they commonly form during slickenside development regardless of lithology or tectonic setting. Our results suggests that 1) PSS likely arise by progressive localization along weaker oriented fabrics 2) deformation along PSS's is energetic enough to comminute the rocks into nanometric grains, and 3) fault geometry can be further characterized by studying the height distributions of fault surfaces, which are likely to impact stress distributions and frictional responses along faults.

Plain Language Summary

Grooved, polished rock surfaces known as slickensides are associated with wear along faults, which makes them useful indicators of the kinematics and grain-scale processes occurring during fault slip. We study naturally formed slickensides from three different faults with different rock compositions. Slickenside surfaces reveal directionally dependent textures with respect to the grooves that exhibit similar patterns over a wide range of length scales, as many other faults do. The slickenside heights, however, do not follow a normal distribution, and the shape of the distributions varies with the scale of observation.

Microscopic observations below the surface show that oriented patterns form next to the slickenside surface with most of the deformation concentrated within a narrow region (≤100 μm) near the surface. This region is mostly composed of ultra-fine particles (≤1 μm) and other frictionally produced films. Our results suggest that 1) such fault surfaces emerge through progressive deformation along ever weakening regions and 2) faults can release enough energy to break the rocks into nano-sized particles during slip. Further, our results highlight additional geometrical information of the surface which can impact how stress is distributed along faults and consequently how faults slip.

1. Introduction

Geologic observations indicate that slickensides—smooth, striated rock surfaces-- and associated fault rocks record motion and mechanical wear between faulted blocks (e.g. Doblas, 1998; Fleuty, 1975; Lyell, 1871; Petit, 1987). The direct imprint of wear recorded along slickensides makes them particularly useful kinematic indicators as well as indicators of the grain scale processes leading to- and occurring during–slip. Studies on natural and experimental fault surfaces have suggested a wide range of processes can be recorded within slickensides and associated fault rocks such as: mechanical amorphization and silica gel formation (Houser et al., 2021; Kirkpatrick et al., 2013; Ohl et al., 2020; Pec et al., 2012, 2016; Rowe et al., 2019; Taylor et al., 2021; Toy et al., 2017), extreme comminution and nanoparticle formation (Di Toro et al., 2011; Houser et al., 2021; Kuo et al., 2016; Ohl et al., 2020; Power & Tullis, 1989; Siman-Tov et al., 2013; Sun & Pec, 2021; Tisato et al., 2012; Toy et al., 2017; Verberne et al., 2014, 2019; Viti et al., 2016), localized frictionally induced heating (Ault et al., 2019; Evans et al., 2014; Houser et al., 2021; Ohl et al., 2020; Rowe et al., 2019; Siman-Tov et al., 2015; Taylor et al., 2021; Toy et al., 2017; Verberne et al., 2014), frictional melting (Magloughlin & Spray, 1992; Nielsen et al., 2010; Spray, 1989, 1992), crystal-plastic deformation (Bestmann et al., 2011; J. Chen et al., 2020; Ohl et al., 2020), rupture propagation direction (Kearse et al., 2019; Macklin et al., 2021) and temporal changes in coseismic slip (Otsubo et al., 2013), highlighting their potential usefulness for deciphering the physico-chemical processes that occur during fault slip. Such observations are crucial for the understanding of the microphysical origins of friction and could eventually lead to constraining microstructural fingerprints associated with high slip velocities, which remains one of the outstanding questions in the study of fault zones (Rowe & Griffith, 2015).

Slickensides further allow us to study and characterize in detail and over many scales the geometry of single fault segments (Bistacchi et al., 2011; Brodsky et al., 2016; Candela et al., 2009, 2012; J.-J. Lee & Bruhn, 1996; Power et al., 1987). This is particularly important as fault geometry has been shown to be a major factor contributing to earthquake rupture nucleation, propagation and arrest (e.g., Ben-Zion & Rice, 1997; Cattania & Segall, 2021; Sagy & Lyakhovsky, 2019; Scholz, 2019; Tal et al., 2020). The irregularities on the surface geometry, known as roughness, exert a direct control on surface properties that control surface interactions such as real area of contact, friction, wear, and lubrication (e.g., Bhushan, 2013; Boneh & Reches, 2018; Bowden et al., 1939; Dieterich & Kilgore, 1996; Tal et al., 2020).

Over the last decades, studies have shown that fault roughness exhibits a self-affine geometry that spans many scales of observation (Bistacchi et al., 2011; Brodsky et al., 2016; S. R. Brown & Scholz, 1985; Candela et al., 2009, 2012; X. Chen et al., 2013; Kirkpatrick & Brodsky, 2014; J.-J. Lee & Bruhn, 1996; Power et al., 1987; Shervais & Kirkpatrick, 2016; Siman-Tov et al., 2015; Toy et al., 2017). In contrast to a self-similar geometry that is scale independent, a self-affine fractal is scale dependent. This means that in order to observe self-similarity, i.e., scale-invariance, an affine transformation that scales the axes of the fractal surface (e.g., length vs. width) differently is needed (Mandelbrot, 1985). Due to current limitations of subsurface imaging techniques, most of our understanding of fault processes relies on the study of exhumed fault surfaces, experiments, and numerical models.

Current fault zone models feature a zone of distributed fracturing with increasing intensity that culminates in a highly strained fault core characterized by an abundance of highly fractured and comminuted fault rocks (Caine et al., 1996; F. M. Chester & Logan, 1986; Faulkner et al., 2010). The architecture of fault zones is then generally described by: a) distribution and number

of cores, b) width and intensity of fracturing within the damage zone, and c) distribution of subsidiary faults (Faulkner et al., 2010, 2011). Fault zones that are currently exposed experienced a number of discrete slip events that ultimately lead to fault zone development (e.g., Gold et al., 2020; Shervais & Kirkpatrick, 2016). Slickensides can form between two shearing blocks and subsequently form prominent fault surfaces. The architecture of a fault zone, structures found within fault zones, and the strain partitioning between them, need to be known so that their potential effect on ground motion can be evaluated. Rupture models typically rely on the interaction of one or few rough fault segments (e.g., Bruhat et al., 2020; Cattania & Segall, 2021; Graves & Pitarka, 2016; Ulrich et al., 2019) with recently developed models accounting for a much larger number of interacting slip surfaces (Chu et al., 2021; Tsai et al., 2021; Tsai & Hirth, 2020).

Thus, this work aims to thoroughly describe the geometry of discrete slip surfaces and identify the dominant deformation mechanisms occurring during slip and slickenside development. We examine the surface and associated microstructures of individual principal slip structures recorded along natural slickensides from three different fault systems hosted within different lithologies. We start by studying the roughness of each slickenside using Fourier Power Spectrum Density analyses (PSD) to derive their respective Hurst exponent, otherwise known as the roughness coefficient. The geometry of the different slip surfaces is further characterized by statistically describing the height distributions of the surfaces at multiple scales of observation. Our work on slickensides is then extended beyond the surface to the fault rocks that host them by conducting detailed microstructural and grain size distribution analyses of the rock volume surrounding the fault surface. Lastly, we discuss the implications of our observation on our understanding of fault processes

2 Methods

We focused on slickenside surfaces collected from 3 different fault systems--a strike slip Plan de los Plátanos fault (PP) in SE Jalisco, Mexico, the Big Piute Ranges low angle normal fault (BP), and Waterman Hills detachment fault (WH), both in SE California-- that represent different lithologies and/or tectonic settings as summarized in Fig. 1. At each locality, we aimed to sample specimens that preserved both sides of the fault surface, if possible, to better capture the structures and materials that comprise slickensides. The faults--PP, BP, and WH-- cut through primarily andesite, quartzite, and mylonitic metasedimentary (*MMS*) rocks, respectively.

2.1 Brief Geologic Background of Analyzed Samples

2.1.1 Plan de los Plátanos Fault

The Plan de los Plátanos is right lateral strike slip fault that accommodates ~430 m of displacement. It is located NW of Autlán de Navarro, Jalisco, Mexico within the Jalisco Block, a rigid tectonic block developed during the Miocene that moves independently from the Rivera and North American plates bounded by the Tepic-Zacoalco Rift and the Colima Rift (De la Teja Segura & Roque Ayala, 2007; Ferrari et al., 2000; Rosas-Elguera et al., 1996). The PP fault is a subvertical structure that cuts through Laramide-folded Tertiary andesite-rhyolite tuffs that overlain the Tepaltepec cretaceous volcano-sedimentary sequence, intruded by the late Cretaceous- early Paleogene Tomatlan granitic batholith (De la Teja Segura & Roque Ayala, 2007).

The PP slickenside sample was collected from a minor splay exposed on the side of the road near the town of Jalocote (De la Teja Segura & Roque Ayala, 2007). The sample records multiple slickenside surfaces hosted in a porphyritic andesite with sericitized plagioclase phenocrysts in the 0.1-1.0 mm range. The rock is hydrothermally altered with secondary chlorite and iron oxides

151 comprising the bulk of the fracture fill along with few quartz-rich veins. Despite the heavy
152 alteration and hosting of slickensides, the host rock seldom records pervasive/distributed
153 deformation as the primary igneous texture is relatively intact a few cm away from the slip surface.
154
155 **2.1.2 Big Piute Normal Fault**
156 The Big Piute Mountains lie in the eastern Mojave Desert within a late Cretaceous ductile
157 deformation belt of synkinematic metamorphism and granitoid pluton emplacement. Thick-
158 skinned thrusting places Proterozoic crystalline basement over recumbently folded Paleozoic
159 meta-sediments. A sequence of Tertiary sedimentary and volcanic rocks overlies Mesozoic,
160 Paleozoic and Proterozoic rocks. Tertiary faults cut through all strata and account for 20-30%
161 crustal extension accommodated in the region (Fletcher & Karlstrom, 1990).
162 Slickensides from this location were collected from small subsidiary faults within the damage zone
163 of the BP that likely accommodated no more than a few meters of displacement. Unlike the other
164 samples, the slickenside in these faults are hosted within a monomineralic quartzite host rock with
165 a primary grain size ranging from 200 μm - 1 mm.
166
167 **2.1.3 Waterman Hills Fault**
168 The Waterman Hill Detachment Fault (WHDF) is a low angle detachment fault thought to
169 accommodate more than 40 km of total slip located within Central Mojave Metamorphic Core
170 Complex exposed along the Mitchell Range N of Barstow, SE California (Glazner et al., 1989).
171 The WHDF juxtaposes Tertiary sedimentary and volcanic strata against Mesozoic granodiorites
172 and the Waterman Gneiss comprised by mylonitized late Proterozoic to Paleozoic
173 metasedimentary and metaigneous lithologies (Fletcher et al., 1999; Glazner et al., 1989).

The samples were collected from a minor fault exposure found within the mylonitic footwall of the WHDF. The fault surface occurs at the lithological boundary of metaigneous, quartzitic and metacarbonate protoliths. The slickensides are hosted within a thick cataclasite (larger than the hand samples) comprising multiple lithologies. The rock itself is overprinted by hydrothermal alteration and calcite-filled fractures.

2.2 Sample Preparation

The collected hand samples were cleaned of any loose debris and dirt prior to any surface measurement. After surface measurements are performed, we prepared 20 thin sections perpendicular to the plane of the slip surface following (Tikoff et al., 2019) orientation convention, where *XZ* and *YZ* correspond to thin sections oriented parallel and perpendicular to the slip lineations, respectively.

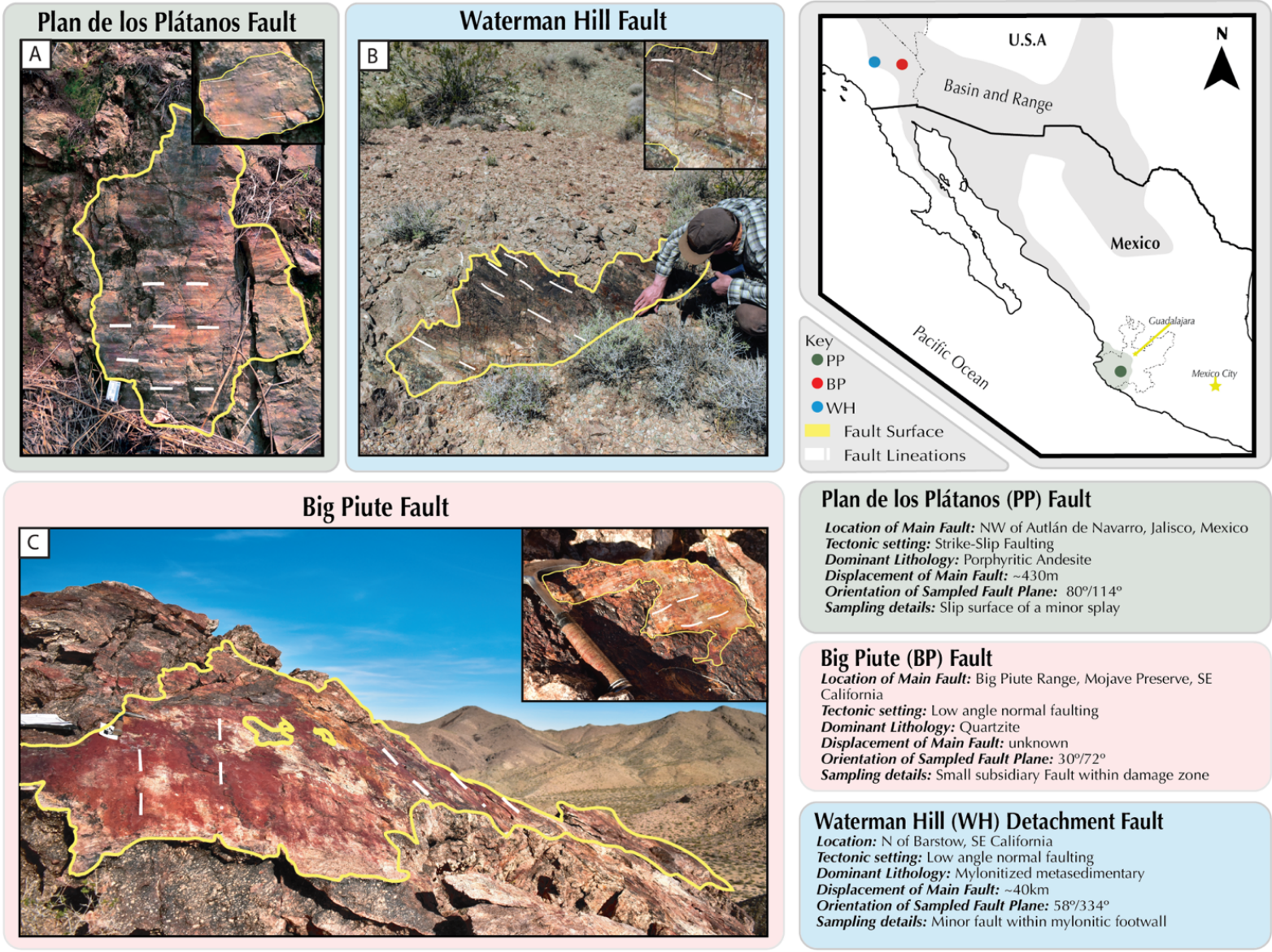

Plan de los Plátanos (PP) Fault

Location of Main Fault: NW of Autlán de Navarro, Jalisco, Mexico
Tectonic setting: Strike-Slip Faulting
Dominant Lithology: Porphyritic Andesite
Displacement of Main Fault: ~430m
Orientation of Sampled Fault Plane: 80°/114°
Sampling details: Slip surface of a minor splay

Big Piute (BP) Fault

Location of Main Fault: Big Piute Range, Mojave Preserve, SE California
Tectonic setting: Low angle normal faulting
Dominant Lithology: Quartzite
Displacement of Main Fault: unknown
Orientation of Sampled Fault Plane: 30°/72°
Sampling details: Small subsidiary Fault within damage zone

Waterman Hill (WH) Detachment Fault

Location: N of Barstow, SE California
Tectonic setting: Low angle normal faulting
Dominant Lithology: Mylonitized metasedimentary
Displacement of Main Fault: ~40km
Orientation of Sampled Fault Plane: 58°/334°
Sampling details: Minor fault within mylonitic footwall

Figure 1. Studied fault surfaces. Yellow line highlights slip surfaces and white dotted lines indicate slip lineations. A) Slickensides at the right lateral strike-slip, Falla de Plan de los Plátanos, ID card for scale (8.56 cm long). B) Minor slip surface cutting through the mylonitic footwall of the WH. C) Subsidiary fault within the BP fault damage zone. Insets are close-ups of sampled regions.

196 **2.3 Roughness analysis**

197 We characterized and quantified the slickenside roughness of the different fault surfaces
198 over six orders of magnitude in length scale ranging from 100's of nm to 3 cm. Each surface
199 (between 100 mm^2 to 1000 mm^2) was measured by a Taylor Hobson TALYSCAN 150
200 profilometer using a no-contact laser gauge with a 252 nm vertical resolution. A constant 2 mm s^{-1}
201 traversing speed and a 5 μm spacing were used for each measurement unless otherwise indicated.
202 At the micron scale, the slip surfaces' topography was measured by manually tracing the surface
203 profile of selected thin sections imaged through Scanning Electron Microscopy (SEM).
204

205 **2.3.1 Hurst Exponent Calculation**

206 The TALYSCAN 150 measurements were processed in MATLAB to remove any planar
207 inclination trend associated with the initial sample placement on the profilometer. 1) The
208 measurements- in the form of an elevation matrix- are then rotated such that the horizontal axis (*x*-
209 axis) of the 3D and digital elevation models (DEM) are parallel to the slip lineations. Once the
210 trend has been removed from the elevation matrices, we proceeded to calculate the Hurst exponent
211 using power spectrum density analyses (PSD) (c.f., Bistacchi et al., 2011; Candela et al., 2009,
212 2012; Jacobs et al., 2017; Siman-Tov et al., 2013). Profiles parallel and perpendicular to the slip
213 lineations are extracted from each surface. A one-dimensional Hann window function is then
214 applied to each line scan to correct for measurement artifacts, particularly near the edges, as
215 suggested by Jacobs et al., (2017). 3) The Fourier power spectrum $P(k)$ is calculated for each
216 profile as a function of wavenumber (k) and normalized by dividing the power spectrum by the
217 length of the corresponding profile. 4) The power spectra for both the parallel and perpendicular

directions to slip are averaged at each wavenumber to reduce noise associated with each individual profile. 5) The Hurst exponent is then calculated from the best fit to a power-law of the form $P(k)=Ck^{1-2H}$, where H is the Hurst exponent, and C is the pre-factor. The workflow is illustrated in Fig. 2.

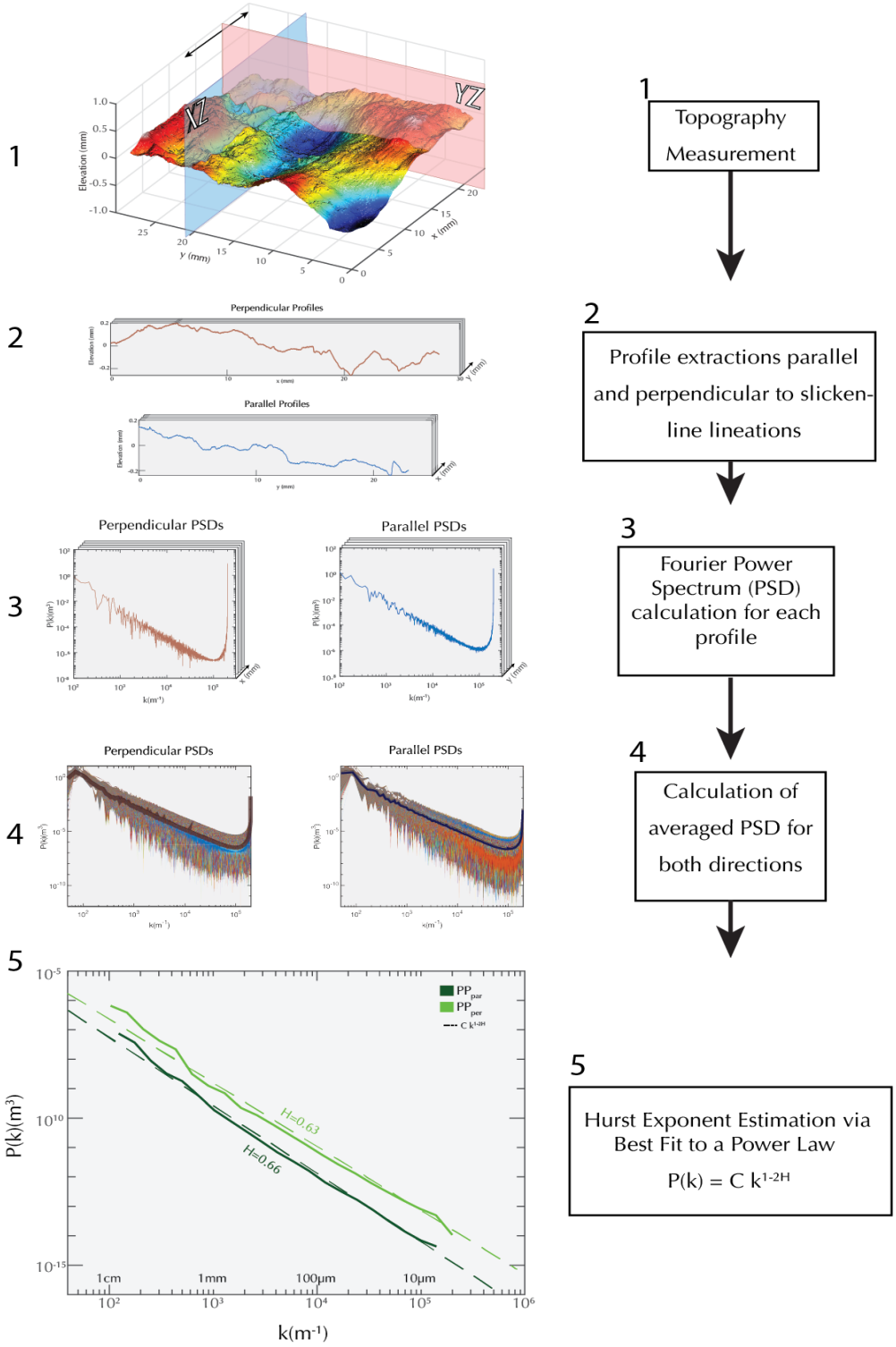

Figure 2. Calculation of Hurst Exponent. See text for details.

2.3.2 Multiscale Surface Texture Analysis

Given that the roughness measurements are inherently a superposition of surface texture information from different length scales, we performed a multiscale surface texture analysis (MSA) in addition to the Hurst exponent calculation. A MSA consists of decomposing the surface topography at various cutoff wavelengths to separate the surface texture into 1) *form*, 2) *waviness* (macro-roughness), and 3) *roughness* (micro-roughness) as shown in Fig. 3 (C. A. Brown et al., 2018). We used a Gaussian 2D filter to separate the data into three different bandwidths with cutoff wavelengths centered at 5 mm and 500 μm. Care is taken that the energy of the signal is preserved, i.e., that the original signal can be fully reconstructed when all components are added together. Furthermore, for each component, we calculate the kurtosis (S_{kur}) and skewness (S_{sk}) of the height distribution.

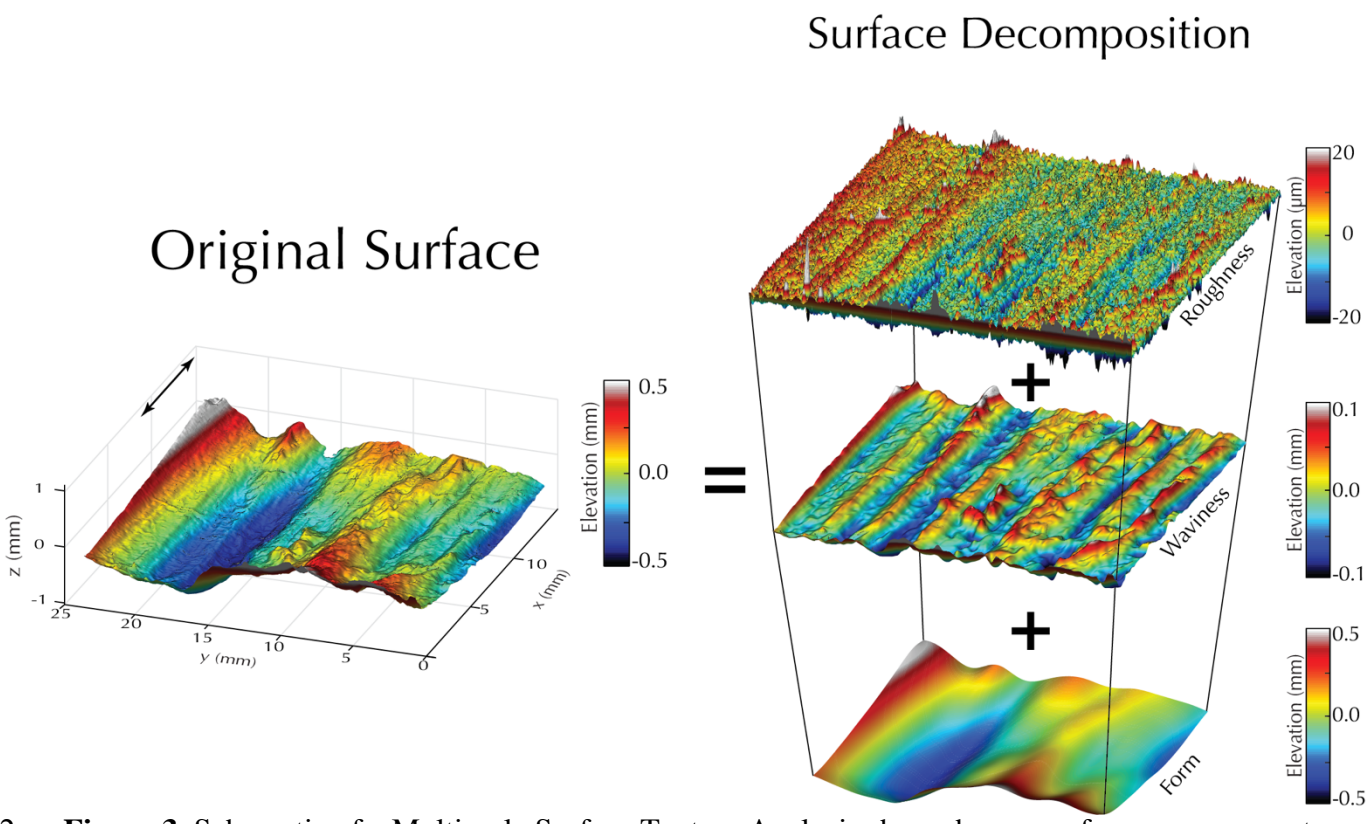

Figure 3. Schematic of a Multiscale Surface Texture Analysis shows how a surface measurement is decomposed into characteristic wavelengths.

2.4 Microstructural Analyses

We aim to identify the microphysical processes occurring within the slickenside volume and adjacent fault rocks. We study a) the grain size distributions and b) the morphologies and crosscutting relationships preserved in, and adjacent to the slickensides to reveal their relationship to fault surface development.

2.3.1 Imaging conditions

Thin sections oriented parallel (*XZ*) and perpendicular (*YZ*) to the slip direction were analyzed using a ZEISS AX10 Petrographic microscope and ZEISS Merlin HR-SEM equipped with a Backscattered electron (BSE) detector.

The SEM was operated with a beam current of 5 nA and a 15 kV accelerating voltage unless otherwise indicated. To capture the range of structures and grain sizes, images were acquired at various magnifications resulting in a 0.77 nm/px to 2.06 μm/px resolution.

2.2.2 Grain Size analysis

Grain size measurements were obtained by manually tracing petrographic microscopy and BSE images obtained at progressively higher magnifications as illustrated in Fig. 4. At each magnification we trace the maximum number of discernible grains/clasts, typically 300-3000 segmented grains per image range are used. Segmented images were then imported to *ImageJ* to calculate the area (A) of each grain in pixels. Grains with areas smaller than 20 pixels, i.e., the smallest grain size that could still be clearly recognized as such, were excluded. The size of each grain is then approximated by calculating the diameter of a circle with the same area. The equivalent diameters (d_{eq}) were calculated as

$$d_{eq} = 2\sqrt{\frac{A}{\pi}}, \quad (1)$$

and collected in a histogram with twenty bins for each magnification.

The bins from each magnification are plotted in a logarithmic scale to determine the slope (S_n) and intercept (I_n) of the best power-law fit. The frequency of each bin is then multiplied by a factor (L_n) that reflects the relative magnification at each image to correct for undercounting of the total number of grains from analyzing progressively smaller areas. The factor, L_n, is determined by:

$$L_n = 10^{I_{max} - I_n}, \quad (2)$$

where I_{max} corresponds to the intercept of the lowest magnification. The results from all magnifications are then combined into a single plot.

D-values of 0-2 are commonly measured in two-dimensional analyses (e.g., analysis of SEM images) and correspond D-values between 1-3 from three dimensional analyses such as sieving and Coulter counting (Glazner & Mills, 2012). To draw comparison with D-values reported in other studies that utilized three-dimensional methods the following conversion, $D_{2D}=D_{3D}-1$, from Heilbronner & Barrett (2014) is used.

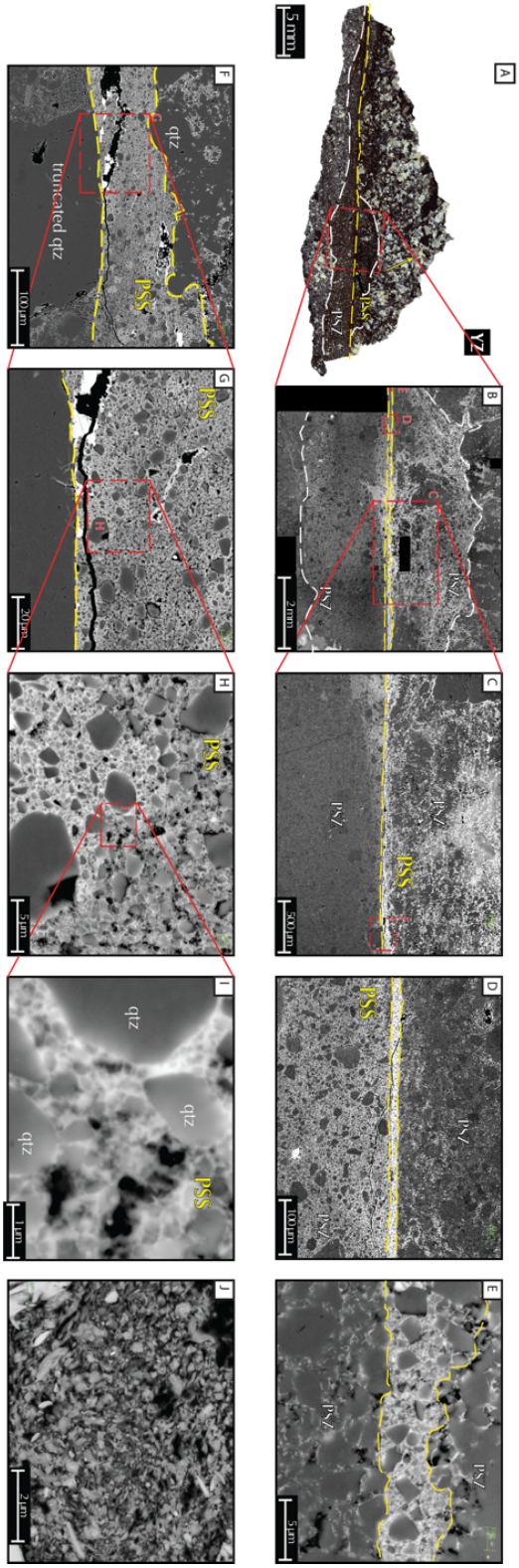

Figure 4. Set of images at progressively higher magnifications used in the GSD determination of quartzite hosted slickenside. See text for details.

3. Results

3.1 Roughness Analysis

Roughness plays a significant role in the contact behavior of surfaces and is usually described as the deviations normal to a surface. We analyzed the roughness of our slickenside samples using the Fourier power spectrum density (PSD) approach to calculate their respective Hurst exponents followed by a multiscale analysis of the surfaces' height distributions.

In Figure 5 we show the wide variety of surface textures that can be qualitatively grouped into two general domains, "*smooth*" and "*rough*", based on the amplitudes and frequency of the dominant asperities.

3.1.1 Power Spectral Density Results

The averaged power spectral density (PSD) curves for all roughness measurements are shown in Fig. 6. PSDs are obtained from profiles scanned parallel (*par*) and perpendicular (*per*) to the slip lineations, i.e., the *x*- and *y*-directions, as illustrated in Fig. 2.

Spectra for most measurements show only limited variability in the slope of profiles measured parallel to lineations with a mean Hurst exponent of 0.53 ± 0.07 and a range of 0.41-0.63. In contrast, the perpendicular profiles showed a wider variability with values of H_{per} ranging from 0.45-0.72 and a mean of 0.60 ± 0.10. The pre-factor is directly proportional to root mean squared roughness (*RMS*) by

$$\boldsymbol{RMS} = \sqrt{\left[\frac{\mathbf{Ck}^{-2H}}{-2H}\right]_{k_{min}}^{k_{max}}} \tag{3}$$

And thus, a higher C indicates overall higher roughness amplitude, whereas a lower H indicates a larger contribution of smaller wavelengths/higher spatial frequency, i.e., surfaces relatively rougher at smaller length scales than a self-similar surface ($H = 1$) with the same C would be. While the samples studied in this paper show a relationship between the pre-factors and H, the inclusion of measurements from Bistacchi et al., (2011) and Candela et al., (2013) indicates no clear trend (Fig 6B). Furthermore, measurements of the various hand samples obtained from the same fault surface show a wide range in both H and C values, Table 1.

Table 1. Hurst (H) and Pre-exponent (C)

Fault	H_{par}	H_{per}	C_{par}	C_{per}
Plan de los Plátanos				
	0.61	0.58	2.5×10^{-3}	2.2×10^{-3}
Big Piute				
Min	0.41	0.45	3.4×10^{-5}	2.2×10^{-3}
Max	0.52	0.72	2.2×10^{-3}	1.8×10^{-2}
Waterman Hill				
Min	0.51	0.48	4.9×10^{-4}	2.2×10^{-3}
Max	0.65	0.71	3.5×10^{-2}	6.2×10^{-2}

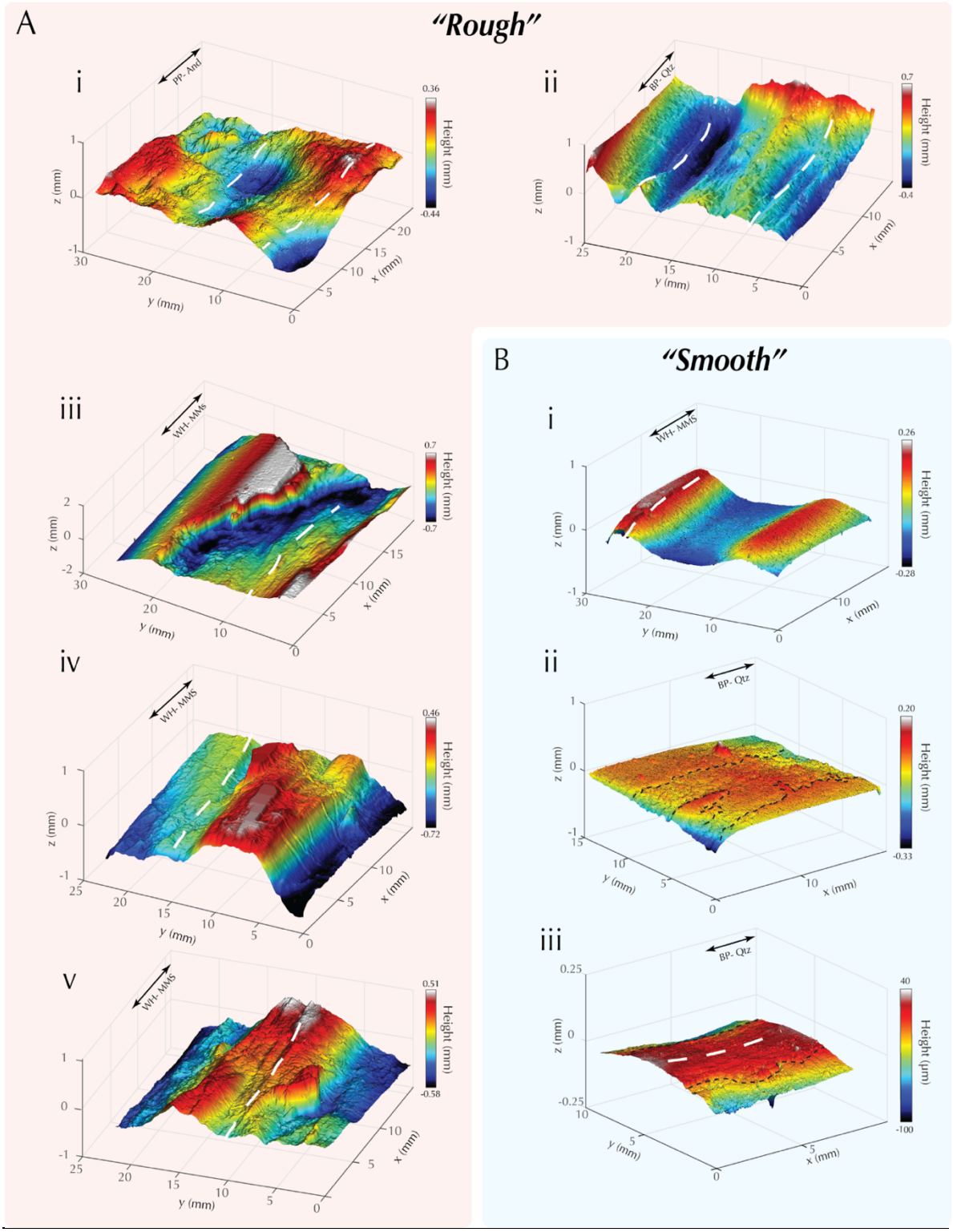
A
"Rough"
i
PP- And
ii
BP- Qtz
iii
WH- MMS
iv
WH- MMS
v
WH- MMS
B
"Smooth"
i
WH- MMS
ii
BP- Qtz
iii
BP- Qtz
Height (mm)
Height (µm)
z (mm)
y (mm)
x (mm)

317

318

319 **Figure 5.** Topography of the different surfaces collected via laser profilometry qualitatively
320 grouped in A) rough and B) smooth surfaces. White dotted lines highlight grooves and lineations.
321 Black dotted lines highlight transitions in roughnesses. PP-, WH-, and BP- indicate the fault
322 system, whereas And (andesite), MMS (mylonitic meta-sedimentary), and Qtz (quartzite) indicate
323 the respective lithologies.

324

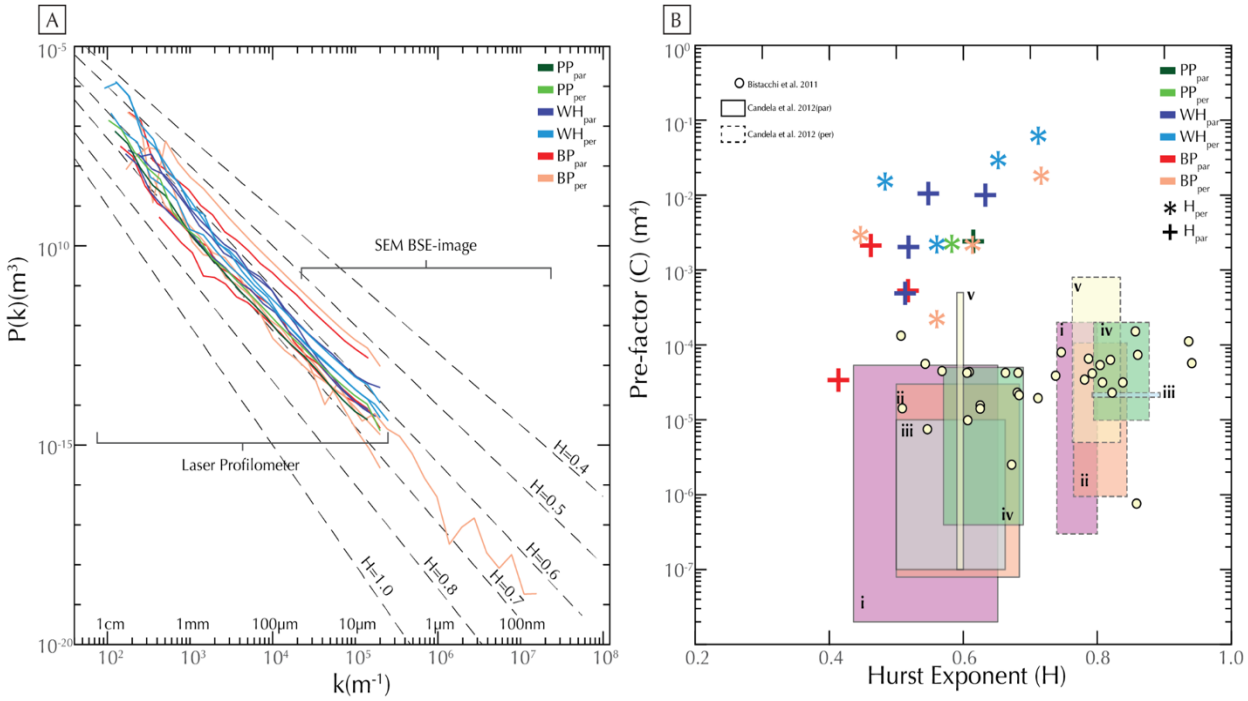

325

326 **Figure 6.** Results from PSD analysis. A) Shows the Fourier power spectra for all studied samples.

327 Note similar slopes fit most samples; rougher samples plot higher in the graph. B) Pre-factor and

328 Hurst exponents obtained from (A), Gole Larghe Fault Zone (Bistacchi et al., 2011) and i) Bolu,

329 ii) Vuache-Sillingy iii) Dixie Valley iv) Corona Heights and v) Magnola faults (Candela et al.,

330 2012). Note data from (Bistacchi et al., 2011) does not specify direction of slip (circles), whereas

331 data from (Candela et al., 2012) is plotted as a range from minimum to maximum values for H and

332 C for both parallel (filled square) and perpendicular (squares with dash lines) directions to slip.

333

3.1.2 Height Distributions

Skewness (S_{sk}) and kurtosis (S_{kur}) are statistical measures that describe the symmetry and peakedness of the height distributions. A distribution is known as a Gaussian when $S_{sk}=0$ and $S_{kur}=3$. A high kurtosis ($S_{kur}>3$) corresponds to a distribution with a greater peakedness than a Gaussian, which indicates more height measurements are centered near the mean height, whereas the converse is true for a low kurtosis ($S_{kur}<3$). Furthermore, a positive and negative skewness indicates most measurements lie either below or above the mean surface, respectively, as illustrated in Fig. 7A. The samples show a wide range of S_{sk} and S_{kur} values, with no systematic variation with respect to lithology or fault system. However, samples wherein lineations are more apparent and visually rougher tend to have more positive skewness whereas, kurtosis is generally higher for smoother samples. The departure from a Gaussian height distribution also appears to be affected by the scale of observation with smaller wavelength having overall higher kurtosis values as documented in Fig. 7A-C. Note also surface decomposition in Fig. 3, which illustrates the distinct roughness at different scales.

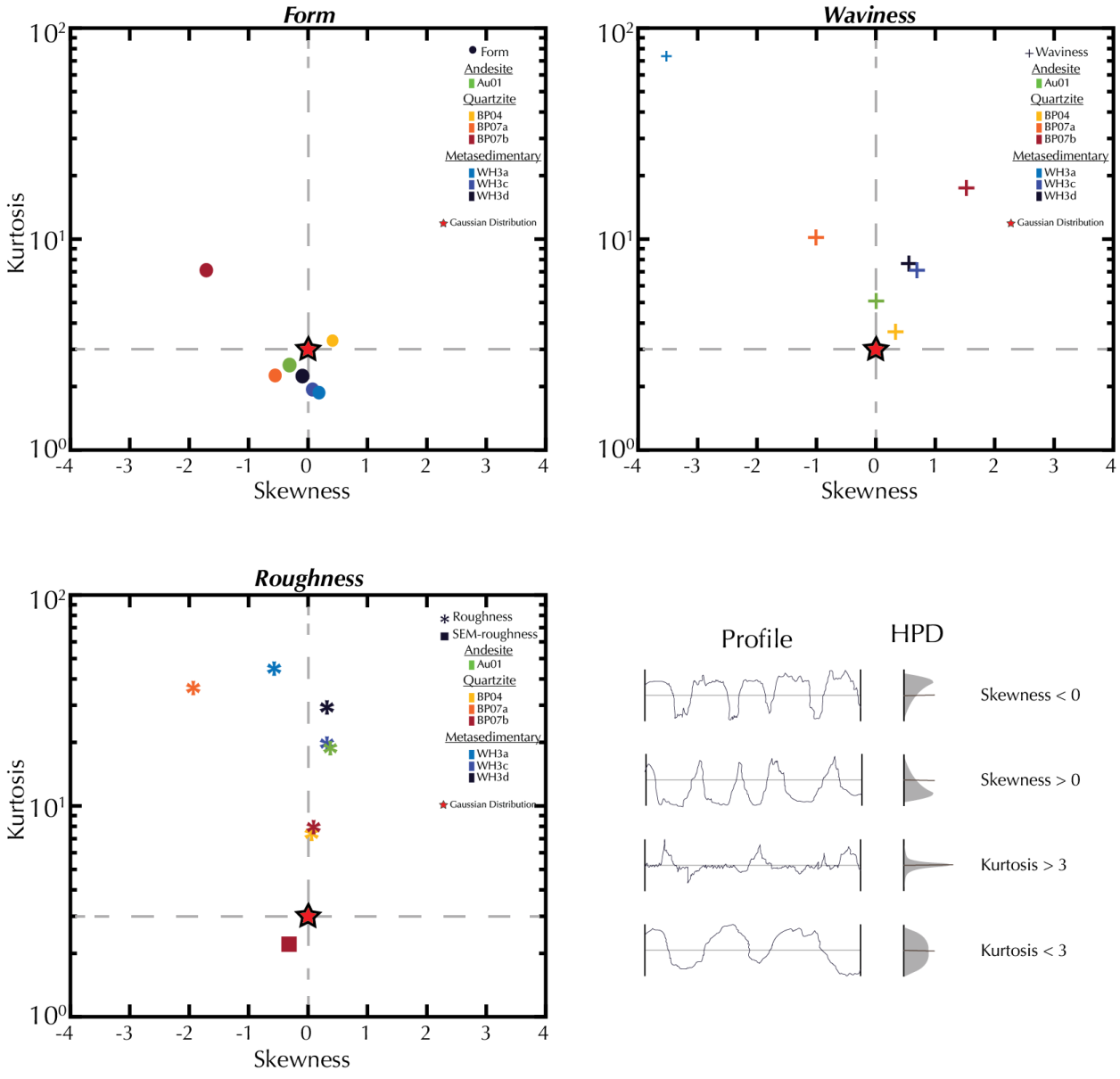

Figure 7. Skewness and kurtosis for samples A) *Form*, B) *Waviness*, and C) *Roughness*. D) Schematic surface profiles with positive and negative skewness and kurtosis values higher and lower than three, after Gadelmawla et al., (2002).

3.2 Structural and Microstructural Observations

With the aim of interpreting the processes involved in fault slip and slickenside development, we selected one sample from each locality that best preserves the slickenside features to conduct SEM-BSE imaging and describe the microstructures in greater detail. We focused on the morphologies at the surface and throughout the rock volume adjacent to the slip surface. For each sample, we specifically examine a) the size and spacing of the lineations, b) orientation of structures on the slip surface, c) the structures within the host rock immediately adjacent to the slip surface, and d) the grain size distribution.

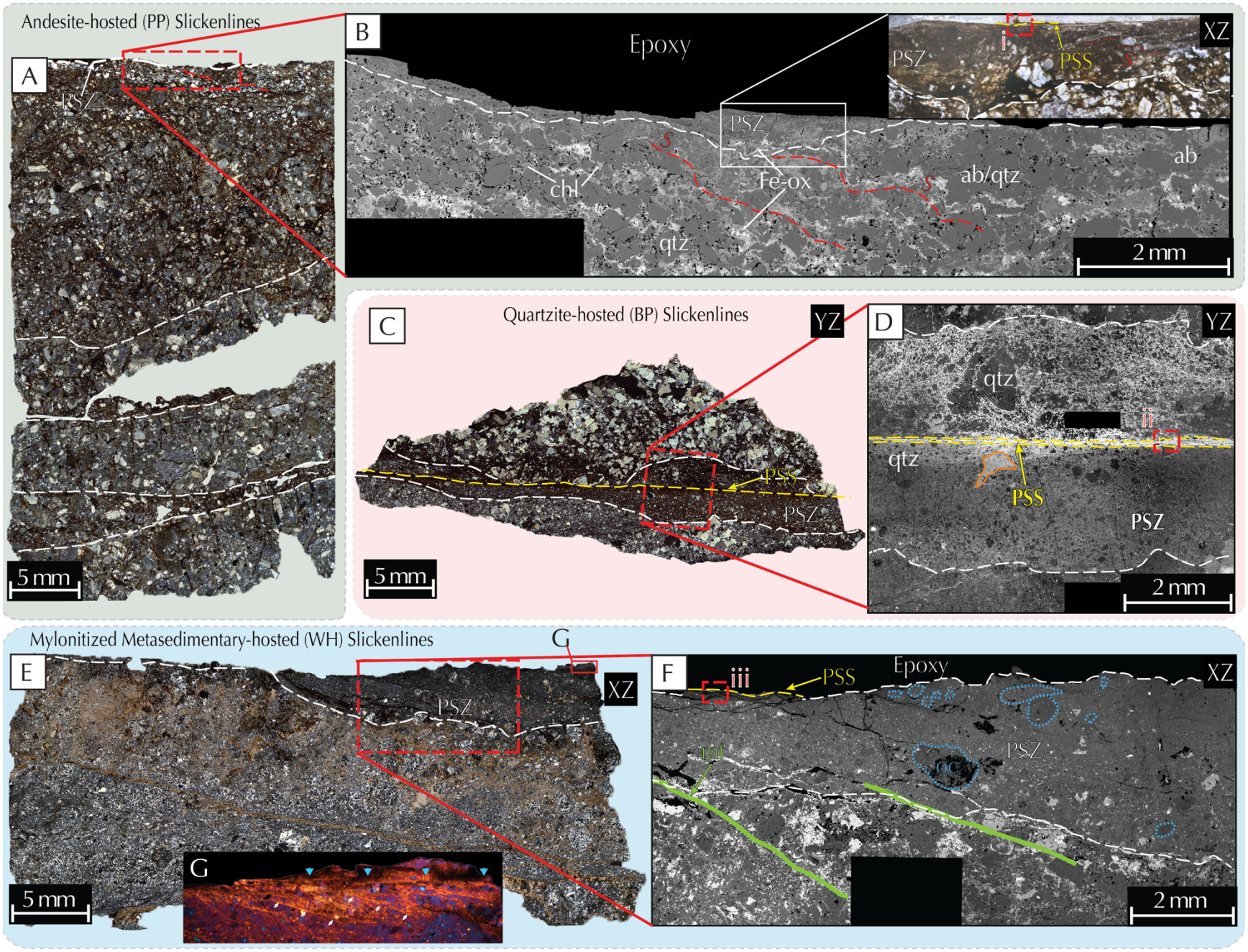
Andesite-hosted (PP) Slickenlines
A
PSZ
5 mm
B
Epoxy
PSZ
S
chl
Fe-ox
ab/qtz
ab
qtz
2 mm
XZ
i
PSS
C
Quartzite-hosted (BP) Slickenlines
YZ
PSS
PSZ
5 mm
D
YZ
qtz
ii
qtz
PSS
PSZ
2 mm
Mylonitized Metasedimentary-hosted (WH) Slickenlines
E
G
XZ
PSZ
5 mm
G
F
iii
PSS
Epoxy
XZ
PSZ
mf
oc
2 mm

Figure 8. Selected samples for microstructural analysis. White and yellow dashed lines highlight Principal Slip Zones (PSZ) and Principal Slip Surfaces (PSS), respectively. A) Andesite hosted slickenside thin sections under cross-polarized light (XPL). Note relatively undeformed primary igneous fabric at the bottom of the image and multiple slip zones. B) SEM-BSE close-up of A. characterized as a zone of highly comminuted grains of irregular thickness. Dark grey colors correspond to quartz (qtz) and albite (ab), bright grey chlorite (chl), white Fe-ox, whereas black spots within the rock volume correspond to porosity. Note S-C cataclasite with top to the left sense of shear. Inset: plane polarized light (PPL) close-up of PSZ fluidized ultra cataclasite. Note tails around larger clasts. C) Quartzite hosted slickensides under XPL, preserving opposing segments of the fault surface. D) SEM-BSE close-up of C. Note the principal slip zone (PSZ) is characterized by highly comminuted grains in the μm-size range, whereas the principal slip surface (PSS-yellow) is localized to few tens of microns and decorated by an abundance of Fe-oxide minerals (bright colors). Note asymmetry in Fe-oxide distribution and comminution between both sides of the fault. Charging artifact denoted by orange lines. E) Slickenside hosted in mylonitic metasediments under XPL. F) Close-up of E shows the presence of a Principal Slip Zone (PSZ) of variable thickness characterized by sharp grain size reduction towards the slip surface and towards a thin Principal Slip Surface (PSS). Note the presence of older cataclastic clasts (OC) within the PSZ. Micro-faults (mf-green) are also observed offsetting the PSZ. G) Close-up of E under XPL with gypsum lambda plate inserted highlights region adjacent to surface where localized shear bands (two main orientations outlined by white and teal arrows) exhibit strong and spatially coherent optical anisotropy.

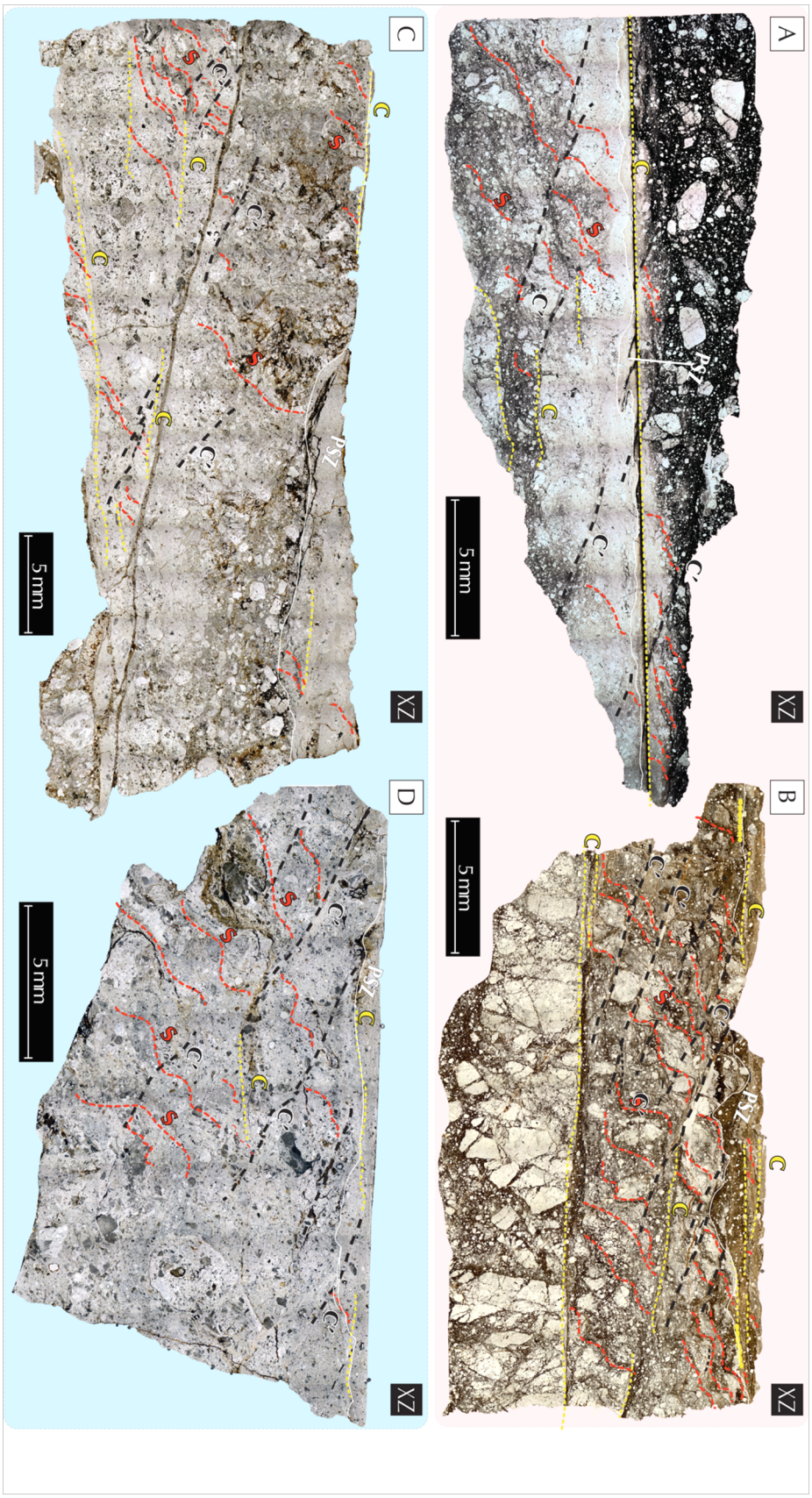

390

391 **Figure 9.** Photomicrographs of foliated cataclasites with S-C-C' fabrics under plane polarized
392 light (PPL). S-, C- and C'- planes outlined by dotted red, yellow, and black lines, respectively.
393 Vertical shaded strips are artifacts from stitching of images. PSZ outlined by thin white dashed
394 line characterized by a sharp decrease in grain size. Note C-planes are parallel to PSS and
395 undulation in PSZ contact follow the edges of S-, C-, and C'-planes. Slickenside hosted in A-B)
396 Quartzite and C-D) mylonitic metasedimentary rocks

3.2.1 Plan de los Plátanos Fault

The main slip surface is covered by a thin film that is glossy and smooth, with specularly reflective patches. The lineations have an average width of 527 ± 83 μm and spacing of 0.85 ± 0.18 mm that remain relatively constant throughout the length of the sample (Fig. 5A). Secondary fractures perpendicular and diagonal to the lineations crosscut the surface.

Below the exposed surface, we identified S-C-like fabrics and a quartz-rich vein with predominantly ductile fabrics that soles into the slip surface. The quartz grains are elongated, exhibit undulose extinction and host multiple inclusions. All fabrics are then cut by a principal slip zone (PSZ) comprising a fluidized ultracataclasite of variable thickness (100-500 μm) that is characterized by a sharp decrease in grain size from the host rock towards the slip surface (Fig. 8A-B). In addition to the main exposed surface, other minor slip surfaces were identified splaying within the sample.

The PSZ features a quartz-rich zone (~10 μm thick) of increased cohesion (ICZ) next to the surface, wherein grains exhibit serrated, interlocked grain boundaries, triple junctions, and sintering microstructures, followed by sharp break towards a ~5 μm thin principal slip surface (PSS) (Fig. 10A and Fig. 11A).

The PSS is characterized by a predominance of mostly rounded submicron-size grains/particles embedded within "*wispy*" phyllosilicate-like matrix enriched in Al and Fe compared to the PSZ (Fig. 10A-Fig 11A). In regions where the PSS is thicker, the PSS exhibits a denser morphology with little to no porosity, albeit fractured, with similarly rounded nm-size grains/particles as well as elongated grains preferentially aligned subparallel to the surface (Fig. 10B).

3.2.3 Big Piute Slickensides

420 The slip surfaces are flat and smooth, i.e., no grooves are perceived with the naked eye,
421 particularly in the direction parallel to the lineations. Iron-oxides (Fe-ox) decorate the slip surfaces,
422 including botryoidal hematite. The lineations are marked by alternating smeared Fe-ox bands with
423 a spacing of 8.2 ± 0.5 mm and 1-3 mm wide grooves (Fig. 5 Bii-iii).
424 Across the XZ orientation, the sample exhibits a foliated cataclasite microstructure with an S-C-
425 C' fabric that transitions into the PSZ and PSS (Fig 9A-B). The foliations are defined by sigmoidal
426 dark brown layers that bound asymmetric quartzite clasts and clast aggregates with their *tails*
427 preferentially oriented ~45º to the fault surface (S-foliation), C'-shear bands developed oblique to
428 the S- and C- orientations, and localized micro-shears sub-parallel to the slickenside surface (C-
429 surface) (F. M. Chester et al., 1985; A. Lin, 2001; Passchier & Trouw, 2005). The waviness of the
430 contact between the host rock and the PSZ follows the orientation of the S-, C-, and C'- planes.
431 The clast size of the cataclasite and spacing between S-C-planes gradually fines and rotate until it
432 transitions into an ultracataclasite that makes up the PSZ and a 18 ± 11 μm thin PSS. (Figs. 8C-D,
433 9A-B, and 10C-D). The PSS is characterized by truncation and plucking of grains from the PSZ
434 and matrix comprising rounded nanometric grains with little to no fractures cemented by a matrix
435 of Fe-ox. Void spaces along fractures within the PSS are then filled by an alternating growth of
436 Fe-ox and quartz, (Fig 10C).
437
438 **3.2.3 Waterman Hill Slickensides**
439 The surface forms a resistant ledge, is smooth and specularly reflective. The lineations are
440 marked by cm-scale undulations within mirror-polished regions and by 520 ± 160 μm wide
441 grooves in portions of the surface that are not specularly reflective.

442 We observe that the WH slickenside samples also exhibit a region of extremely comminuted
443 grains, PSZ, adjacent to the slip surface, and S-C-like fabrics throughout its host rock. Unlike the
444 other samples, the PSZ here varies significantly in thickness, from ~100 μm to 5 mm, along the
445 direction of slip (*XZ*). Regions where the PSZ is thicker coincide with numerous micro-faults that
446 displace the PSZ but do not crosscut the mirror-polished surface. The PSZ contains clasts of earlier,
447 more consolidated cataclasites (OC). Immediately adjacent to the slip surface, two main features
448 are prominent: a) the presence of Reidel-like and boundary (subparallel to the slip surface) shear
449 bands that exhibit extreme grain size reduction and uniform optical anisotropy, Fig. 8E, and b) a
450 dense thin film (PSS) that coats the PSZ that features elongated grains preferentially oriented
451 subparallel to the surface embedded within a potentially partially amorphous matrix, Fig. 10F,
452 similar to Fig. 10B. Nanosized grains are also observed to be common within the matrix of the
453 PSZ.
454

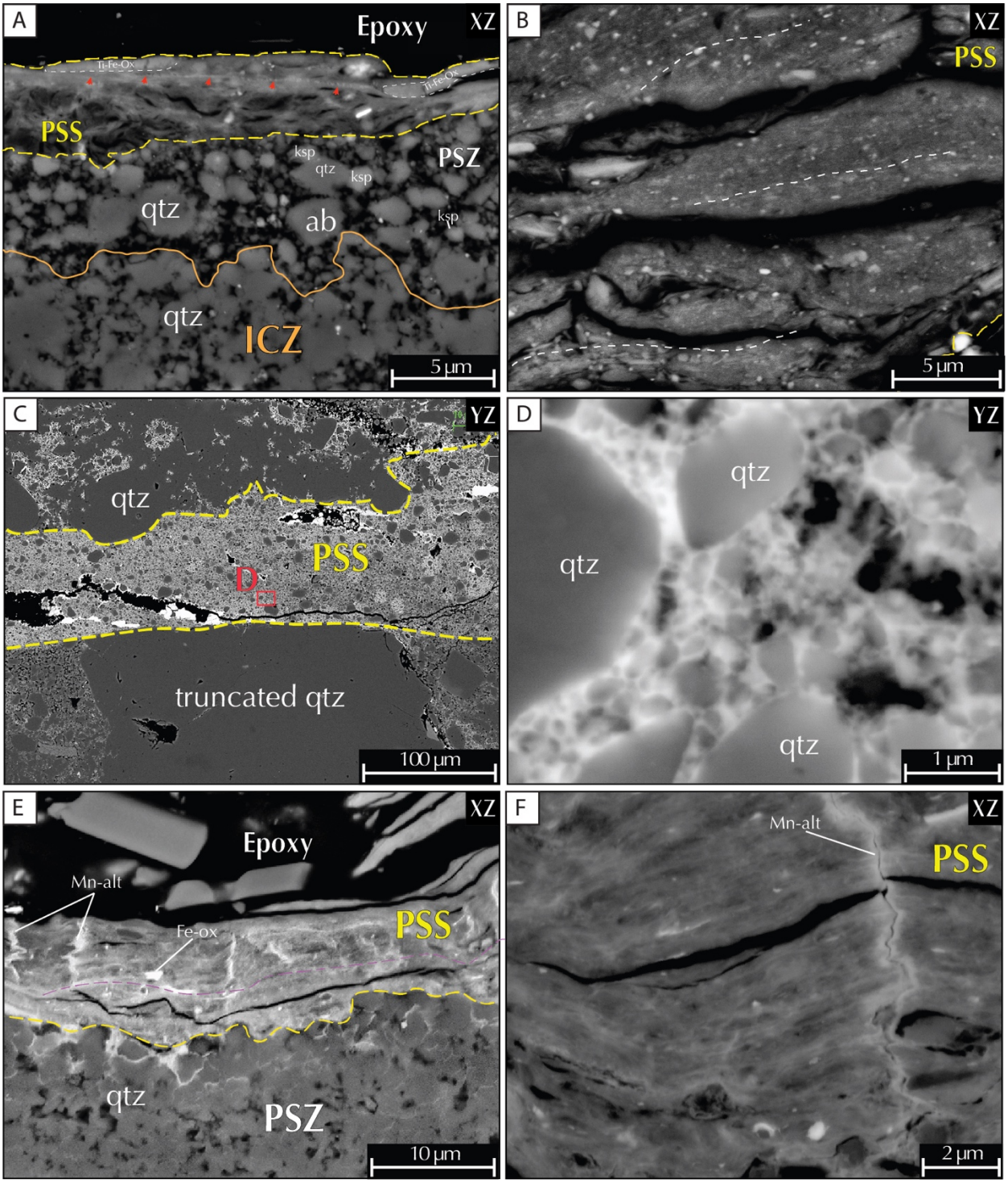
A
Epoxy
XZ
Ti-Fe-Ox
Ti-Fe-Ox
PSS
ksp
qtz
ksp
PSZ
qtz
ab
ksp
qtz
ICZ
5 µm
B
XZ
PSS
5 µm
C
YZ
qtz
PSS
D
truncated qtz
100 µm
D
YZ
qtz
qtz
qtz
1 µm
E
XZ
Epoxy
Mn-alt
Fe-ox
PSS
qtz
PSZ
10 µm
F
XZ
Mn-alt
PSS
2 µm

455

456

Figure 10. SEM-BSE images of the Principal Slip Zones. **Andesite hosted slickensides:** A-B) SEM-BSE operated with 20 kV accelerating voltage and 8.0 nA beam current. A) Close-up of PSZ in Fig 8B.i, showing the presence of a thin PSS and a quartz-rich Increased Cohesion Zone (ICZ) and PSS. Note the PSS is a thin layer (a few microns thick) comprising a randomly oriented Al- and Fe-rich "wispy" phyllosilicate-like matrix and submicron sized particles. Note the roundness of most clasts and Fe-rich veinlet in PSS, red arrows. The ICZ is characterized by a decrease in porosity, grains with irregular and serrated grain boundaries, and sintering microstructures. B) Close-up of dense region of PSS. Note the presence of rounded nano-sized particles and elongated preferentially oriented grains, highlighted by white dashed lines. **Quartzite hosted slickensides:** C) Close-up of the PSS from Fig 8D.ii. Image shows a sharp decrease in grain size from the PSZ (outside of the yellow boundary) towards the PSS, which is characterized by a Fe-oxide-rich layer of micron-sized grains supported in a fine grain matrix. Note truncation of quartz clast by the PSS. D) Close-up of PSS matrix shows matrix comprises predominantly submicron-sized qtz grains and Fe-ox cement (bright colors). Note roundness and lack of fractures on matrix grains and euhedral growth of Fe-oxide blades into void spaces. **MMS hosted slickensides:** E) Close-up into the PSS Fig 8F.iii, shows it comprises a dense layered possibly amorphous matrix with rounded grains and preferentially oriented elongated grains. Note bright vertical features enriched in Mn. Layering is highlighted by a magenta dotted line. F) Close-up of PSS. Note dense matrix with little to no porosity and sub-micron rounded grains.

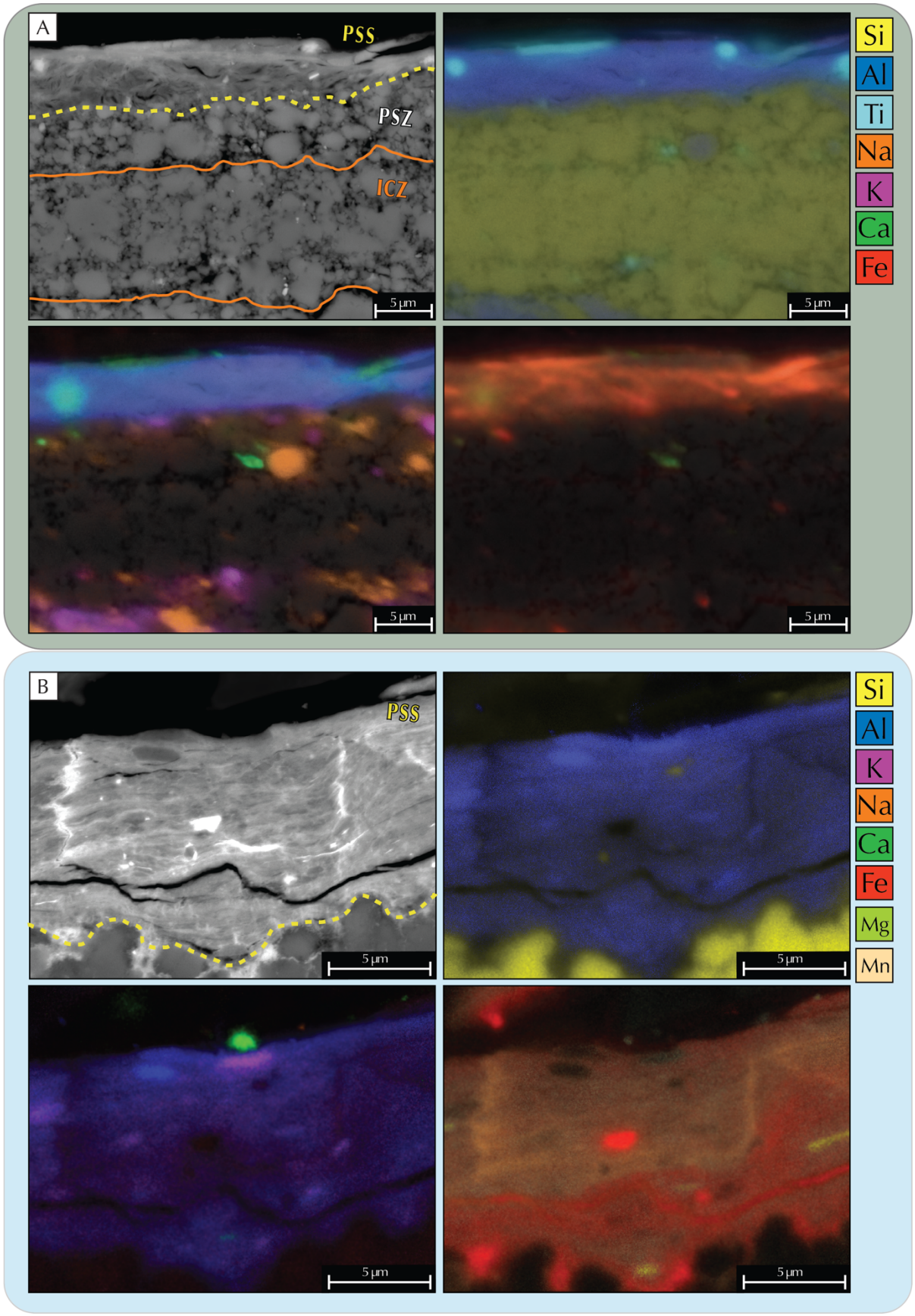

476

Figure 11. Compositional EDS maps of Principal Slip Surfaces. A) Andesite hosted slickensides: from Fig. 10A Note Si-rich (quartz) Increased Cohesion Zone (ICZ) and Al, Fe and Ti enriched PSS. B) MMS hosted slickensides: Close-up of PSS in Fig 10E showing PSS is enriched in Al, Fe. Bright fractures enriched in Mn. Note thin Al-, K-, and Mg-rich rods preferentially aligned subparallel to the slip surface.

3.3 Grain Size Distribution

To characterize the comminution processes occurring during slip, we analyzed the grain size distribution of the fault rocks adjacent to the slip surface. Here we present the results of the grain size analyses performed on two sequences of petrographic microscopy and SEM images taken at increasing magnifications from selected samples from the BP and PP faults. The results are plotted on log-log plots of frequency vs. equivalent diameter to determine the fractal grain size distribution (GSD), Fig. 12.

We did not perform grain size analysis on samples from the WH Fault. It was not possible to accurately identify individual grain boundaries as the particles appear embedded within a cement of similar composition. Furthermore, when the boundaries between particles could be accurately identified, they exhibit interlocked grain boundaries, suggesting static crystal growth and healing (Keulen et al., 2008), and thus obscuring the grain sizes related to the comminution process.

The grain size distribution for the quartzite sample shows a power-law functional relationship over six orders of magnitude (10's nm-1's mm) with a constant slope *of* $D = 2.67 \pm 0.03$ despite the sharp decreases in grain size observed within the transition from the host rock towards the PSZ and PSS respectively, Fig. 8C-D. However, it is observed that at the lower grain size range (less than 100 nm), the distributions start to plateau as the grain size approaches the resolution limit of the SEM (a single pixel at the highest magnification equals 0.77 nm). The smallest grain sizes are found within the unconsolidated gouge with an equivalent $d_{min} = 18\ nm$, whereas the smallest observable grains within the matrix of the PSS corresponded to 30 nm.

In contrast to the monomineralic quartzite, the andesite hosted slickensides exhibit two distinct parts that can be discriminated by a break in the GSD slope. Two *D*-values are obtained: a lower, $D_{<} = 2.05 \pm 0.19$ for small grain sizes ($d<d_k$), and $D_{>} = 2.72 \pm 0.06$, for large grain sizes ($d > d_k$),

505 where $d_{k.} \approx 2\ \mu m$ and is the grain size at the intersection of the two curve fits. This intersection (dk)

506 occurs where grains measured only in the PSS and PSZ overlap. Within the small grain size range,

507 the smallest grains are found embedded within the PSS matrix with a $d_{min}=30\ nm$.

508

509

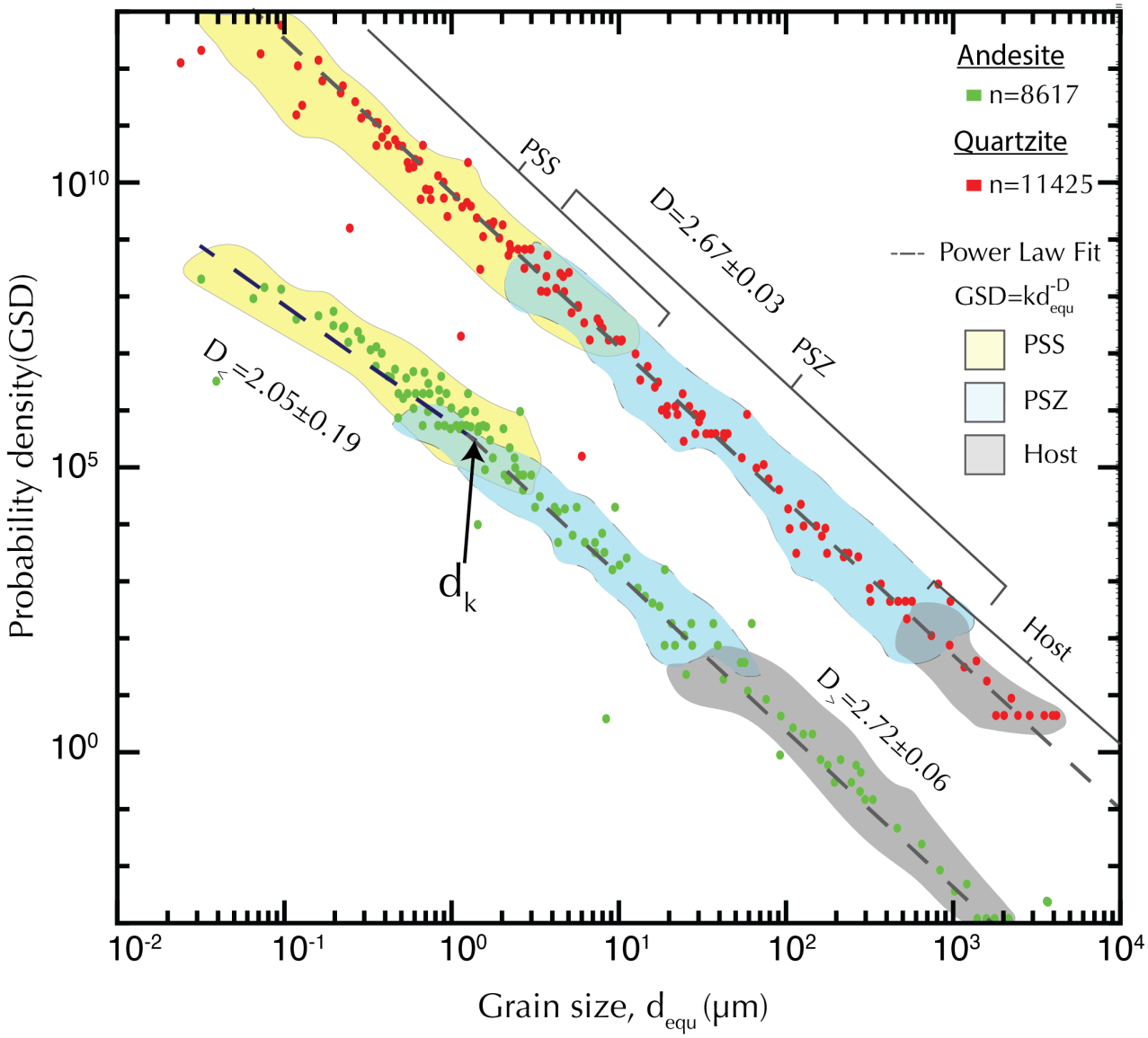
Andesite
n=8617
Quartzite
n=11425
Power Law Fit
GSD=kd^-D_equ
PSS
PSZ
Host
PSS
PSZ
Host
D=2.67±0.03
D<=2.05±0.19
D>=2.72±0.06
d_k
Probability density(GSD)
Grain size, d_equ (μm)
10^10
10^5
10^0
10^-2
10^-1
10^0
10^1
10^2
10^3
10^4

510

511

Figure 12. Grain Size Distributions of quartzite (red) and andesite (green) host rocks. Data has been displaced vertically for clarity. The GSD of quartzite samples can be described by a single $D = 2.67 \pm 0.03$, whereas GSD has two distinct slopes for $D_< = 2.05 \pm 0.19$ and $D_> = 2.72 \pm 0.06$ for grain size smaller or larger than $d_k \approx 2\ \mu$m, respectively. The different color envelopes indicate the range of grain sizes found within the PSS, PSZ, and the host rock. Data points outside the color envelopes correspond to artifacts due to the limited resolution in each measured image.

4 Discussion

This work provides a detailed study of surface roughness of slickensides and the associated microstructures in the surrounding fault rocks from three different fault zones hosted in various rock types that have experienced different deformation histories. The observations from both the surface and respective volume and their implications for our understanding of faulting processes are discussed below.

Fully characterizing a fault surface is of particular importance for better understanding fault processes. It has been shown that the stress distribution is affected by fault geometry, as the latter controls to a first degree the real contact area (e.g., Ben-Zion & Rice, 1997; Bruhat et al., 2020; Cattania & Segall, 2021; Harbord et al., 2017; Sagy & Lyakhovsky, 2019; Tal et al., 2020). Our current understanding of fault surface geometry is that it is self-affine and that it can be characterized by four parameters ($H_{per,}$ $H_{par,}$ $C_{par,}$ C_{per}) (Brodsky et al., 2016; Candela et al., 2009, 2012). In agreement with other reports, our studied fault surfaces further indicate that regardless of lithology or tectonic setting, the roughness of individual fault surfaces exhibits an anisotropic self-affine topography with Hurst exponents (H) and pre-factors (C) within the 0.4-0.8 range and 10^{-5} - 10^{-2}, respectively. The surface roughness of our samples, however, consistently exhibited smaller H-values and less anisotropy than most reported natural fault surfaces, i.e., the roughness measured perpendicular- and parallel to the slip lineations exhibited closely valued Hurst exponents with mean $H_{par}=0.53 \pm 0.07$ and. $H_{per}+0.60 \pm 0.10$ as opposed to the more commonly reported $H_{par}\approx0.6$ and $H_{per}\approx0.8$, (Bistacchi et al., 2011; Candela et al., 2009, 2012; Power & Tullis, 1989; Renard et al., 2012; Sagy et al., 2007; Thom et al., 2017; Tisato et al., 2012). The smaller H

543 values likely indicate that our surfaces appear smoother at larger scales and rougher at finer scales
544 than other faults while the reduced anisotropy could be related to inherent heterogeneity within the
545 fault surfaces. Similarly, this discrepancy could also be related to the conditions at which such
546 surfaces were formed and/or altered. While intriguing, our current observations cannot explain this
547 peculiarity.
548
549 In addition to describing fault surface geometry via fractal descriptors ($H_{per,}$ $H_{par,}$ $C_{par,}$ C_{per}),
550 this work includes multiscale analyses (MSA) on the height distribution of fault surfaces. Our
551 results suggest the kurtosis and skewness of such distributions deviate from Gaussian with a
552 noticeable dependence on the scale of observation, which contrast to some of the models used in
553 earthquake simulations that typically assume faults as Gaussian self-affine rough surfaces (e.g.,
554 (Cattania & Segall, 2021; Graves & Pitarka, 2016). The latter has important implications on our
555 understanding of the role of geometry in faulting processes, as studies on the contact behavior of
556 non-Gaussian surfaces have reported that roughness parameters skewness and kurtosis correlate to
557 noticeable effects on tribological properties such as: friction, wear, mean asperity pressure, and
558 contact area (Ghosh & Sadeghi, 2015; Gu et al., 2021; Kim et al., 2006; Kotwal & Bhushan, 1996;
559 McCool, 1992; Sedlaček et al., 2012; Tayebi & Polycarpou, 2004; Tomota et al., 2019; W.-Z.
560 Wang et al., 2006; Yan et al., 2014; S. Zhang et al., 2014) and fluid transport properties (M. Wang
561 et al., 2016). Thus, further measurements of fault surfaces that also characterizes the distribution
562 of their heights in addition to their fractality seem crucial for more accurate representations of fault
563 roughness in models that explore the role of geometry on seismic slip.
564

While this simplification of fault zones into self-affine rough surfaces is useful for making educated predictions of fault surface geometry at scales and locations not accessible with the current technology (subsurface faults), it is worth noting that wear and therefore slip on a fault cannot be entirely explained by two rough surfaces sliding past each other. Firstly, microstructural observations near single fault surfaces have reported the presence of a discrete zone that concentrates strain and wear comprising extremely comminuted layers with an abundance of nanoparticles and/or other types of tribofilms, within the PSZ and PSS (Ault et al., 2019; De Paola, 2013; Dor & Reches, 2005; Goldberg et al., 2016; Heesakkers et al., 2011; Houser et al., 2021; Kuo et al., 2016; Ohl et al., 2020; Otsubo et al., 2013; Pec et al., 2016; Power & Tullis, 1989; Rowe et al., 2019; Shervais & Kirkpatrick, 2016; Siman-Tov et al., 2013, 2015; Taylor et al., 2021; Tisato et al., 2012; Verberne et al., 2014, 2019; Viti et al., 2016), suggesting that individual fault surface evolution and wear could be better modeled by what is known in tribology as third-body wear (Boneh et al., 2014; Boneh & Reches, 2018; Brodsky et al., 2020; Milanese et al., 2019). More importantly, however, geologic and experimental observations from the submillimeter to kilometers scale indicate that fault zones involve the interaction several structures, with multiple anastomosing fault strands occasionally crosscutting each other (Faulkner et al., 2003; Rowe et al., 2018; Shervais & Kirkpatrick, 2016; Swanson, 1988; Torabi et al., 2020, 2021). For instance, observations of individual natural slickensides and their respective host rocks reveal an intricate set of structures that document progressive localization of strain into what eventually become multiple principal slip surfaces on which subsequent sliding takes place. Specifically, most samples exhibited foliated cataclasites with S-C-like fabrics, with clasts progressively becoming finer toward the C-plane-parallel principal slip surfaces as documented in Fig.9, similar to the structures reported along the PSS of numerous other fault zones (Berthé et al., 1979; Hippertt,

588 1999; Jordan, 1987; Kirkpatrick & Brodsky, 2014; Y.-J. Lee, 1991; A. Lin, 2001; S. Lin et al.,
589 2007; S. Lin & Williams, 1992; Nakamura & Nagahama, 2002; Ortega-Arroyo, 2017). Such
590 observations suggest that development of the PSS is preceded by formation of progressively
591 mechanically weaker zones along which strain is further localized. A simple sequential model is
592 proposed in Fig. 13 based on the observations from natural slickenside samples, analogue
593 experiments with no pre-cut fault surfaces (Will & Wilson, 1989; C. J. L. Wilson & Will, 1990)
594 and numerical modeling (Finch et al., 2020). Therefore, in our interpretation the exposed slip
595 surfaces are the end product of fault slip and wear on fault zone and not the initial conditions on
596 which slip initiate.

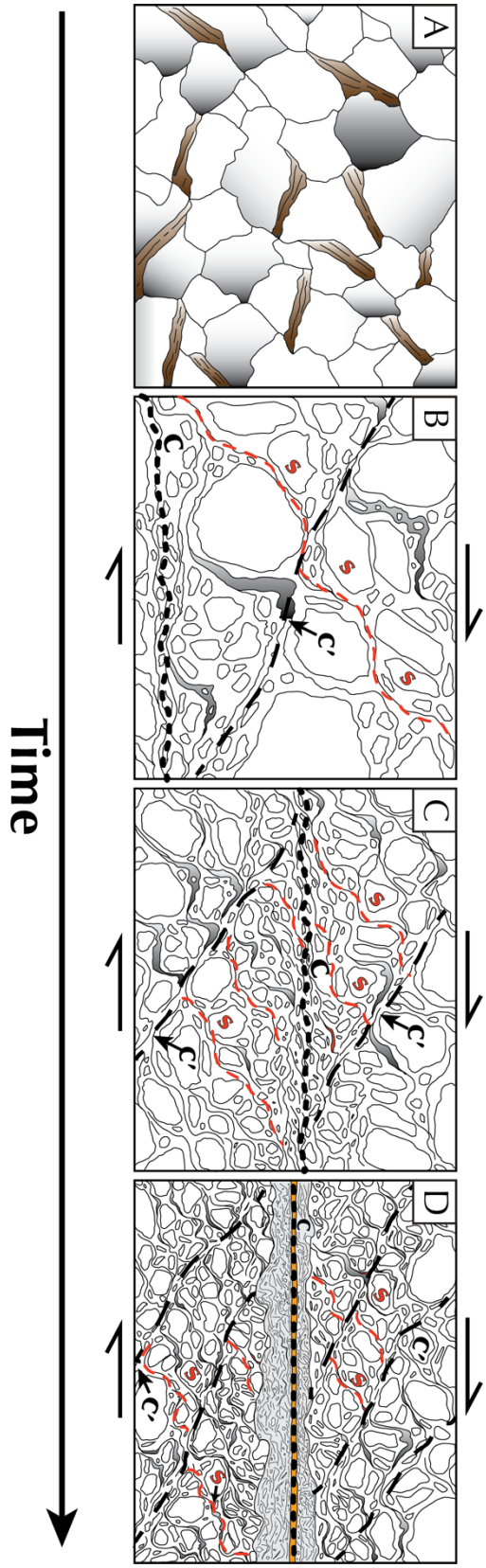

597

598 **Figure 13**. Schematic sequential model of slickenside development. A) Initial undeformed rock.
599 B) S-C-C' fabrics start developing at low -intermediate strain levels. Note S-foliation (red-dashed
600 lines) is defined by asymmetrical clast and clast aggregates with their tails oriented at about 45º to
601 the C-surface (black-dotted lines), whereas C'-shear bands appear oblique orientations (black-
602 dashed lines). C) As shearing continues more S-C' fabrics propagate throughout the sample and
603 create rheologically weaker regions via grain size reduction that preferentially rotate towards C-
604 planes. D) Strain further localizes along the C-planes in the form of finely comminuted material
605 observed in the PSZ (grey) and PSS (yellow)
606

607 At low to intermediate strain, deformation is accommodated via incremental development of
608 oriented fabrics along S-C structures (Will & Wilson, 1989; C. J. L. Wilson & Will, 1990). At
609 higher strains, passive rotation of S-planes into C-planes becomes a more efficient way to
610 accommodate strain over creation of new planes, (Berthé et al., 1979; Finch et al., 2020; Hippertt,
611 1999; Jordan, 1987), which create rheologically weaker regions that accommodate higher strain
612 rates (Finch et al., 2020) and can progressively link with each other to form through going shear
613 zones (Finch et al., 2020; Pec et al., 2016; Will & Wilson, 1989; C. J. L. Wilson & Will, 1990),
614 akin to the process zone suggested by (Cox & Scholz, 1988). The development of these localized
615 shear zones also facilitates infiltration of fluids, as seen in the ubiquitous concentration of
616 secondary minerals and/or alteration products (mainly Fe-ox) along the PSZ and PSS, Figs. 8-11,
617 that likely cause further weakening and slip due to metasomatic reactions and pore pressure effects.
618 The latter suggests an extreme degree of strain localization, where most of the deformation is
619 accommodated by extreme comminution along thin kinematically favorable regions, generally a
620 few tens of microns thick, as documented in Figs. 8-10.
621 To better characterize the extreme comminution processes affecting our samples we performed
622 grain size analyses. Interestingly, the way the grain sizes are distributed appears to vary between
623 the andesite and the quartzite sample. For instance, the slickenside within the quartzite shows a
624 GSD that can be described with a single D value for over six orders of magnitude, whereas the
625 andesite GSD has a break in slope near $d_k \approx 2\ \mu$m, Fig. 12. Grain size measurements from other
626 polymineralic natural and experimental fault rocks have also reported a break in the slope of their
627 GSD at similar critical grain sizes d_k that suggest a change in the dominant comminution
628 mechanisms with attrition and shearing becoming more important at values lower than d_k, usually
629 attributed to the grinding limit (Billi & Storti, 2004; F. M. Chester et al., 1993; J. S. Chester et al.,

630 2005; Keulen et al., 2007). Our quartzite sample does not exhibit this transition and is in contrast
631 to what Keulen et al., (2007) reported for quartz grains in other polymineralic gouges. There could
632 be multiple explanations for the discrepancies at these scales. Firstly, the difference could be
633 related to different breakage mechanisms at sub-micron scale associated to the parent mineralogy
634 (Knieke et al., 2011), as the observations reported in 0Keulen et al., (2007) were done on granitoid
635 lithologies and ours on quartzite and andesite. Moreover, the break in slope observed in the
636 andesite GSD could be related to changes in material properties likely caused by mechanochemical
637 and/or tribochemical reactions acting along the friction zone, PSS, as the d_k appears at the transition
638 where their grain sizes overlap between the PSZ and PSS, (Knieke, 2012; Knieke et al., 2011;
639 Romeis et al., 2016). It is possible that partial mechanical amorphization is among some of the
640 reactions occurring within the PSS, which could help explain the distinct textures observed along
641 the PSS and its GSD. For instance, the dense portion of the PSS, Fig 10B,E,F , exhibits similar
642 textures to those observed along the silica layer within the slickensides studied by Taylor et al.,
643 (2021), wherein Fe-ox nanorods are embedded in a partially amorphous matrix, while the "wispy"
644 microporous matrix, observed in Fig. 10A, resembles the textures reported from hydrothermally
645 altered quenched frictional melts in (Fondriest et al., 2020) likely representing portions that have
646 undergone more advanced hydrothermal alteration with formation of clay minerals, (e.g., Fe-
647 smectite). Furthermore, observations of coeval amorphous and nanocrystalline material are not
648 uncommon along high strain frictional interfaces and have been widely reported along natural fault
649 surfaces (Ault et al., 2019; Houser et al., 2021; Kirkpatrick et al., 2013; Kuo et al., 2016; Ohl et
650 al., 2020; Verberne et al., 2014, 2019; Viti et al., 2016), rock deformation experiments (Kaneki et
651 al., 2020; Marti et al., 2020; Pec et al., 2012, 2016; Pec & Al Nasser, 2021; Toy et al., 2017), and
652 deformation of engineering materials (Han et al., 2012; Viat et al., 2017; Y. S. Zhang et al., 2014;

Zhao et al., 2016), indicating that both nanocrystalline and amorphous material are common products during frictional wear processes regardless of the parent material, and an important component to consider when studying rheology of faults. Nanocrystalline fault rocks are inherently weaker than their microcrystalline counterparts and therefore can form in-situ weak layers along which strain further localizes (Sun and Pec 2021).

Alternatively, both GSD's could also represent different stages in the comminution process as recent studies in confined comminution of granular materials using a simple Discrete Element Models (DEM) and Apollonian gasket models suggest that the GSD continuously shifts as the porosity is reduced until it reaches an ultimate power law that also determines the ultimate contact force distribution (Ben-Nun et al., 2010). Based on the microstructure of each sample it is possible that the observed changes relate to different degrees of comminution. Similarly, Knieke et al. (2009) work on ultrafine particle (nm-range) production with stirred media mills on a variety of different materials shows that the ultimate size that a particle can be broken into, i.e., grinding limit, depends on a multitude of variables including stressing types, the material of the particles to be milled as well as the size and material of the milling particles, and solvents (e.g., hydrous fluids). Thus, the ultimate particle distribution observed along comminuted rocks could reflect the conditions during grinding.

5 Summary and Conclusions

We investigated the surface roughness and associated microstructures of natural slickenside samples from three different fault systems hosted in andesite, quartzite and mylonitic meta-sedimentary lithologies. We found that in addition to exhibiting the usually reported self-affine roughness, with mean $H_{par}=0.53 \pm 0.07$ and. $H_{per}+0.60 \pm 0.10$, all surfaces exhibited non-Gaussian height distributions with noticeable scale-dependence on their S_{kur} and S_{sk} roughness parameters. While our dataset is limited to the shorter length scales associated with fault surface roughness, further studies at a wider range of scales could help constrain the type of height distributions common to natural faults. Moreover, our microstructural analyses suggest such surfaces are likely the product of progressive strain localization and partitioning along regions with high degree of fabric development (S-C-C'- fabrics) that culminate in multiple principal slip zones throughout the samples identified by a sharp decrease in clast size and thin ($\lesssim 100\ \mu$m) principal slip surfaces wherein nanosized particles are abundant along with other tribofilms and reaction products. The prevalence of nanoparticles observed within fault zones regardless of lithology or tectonic setting urges the need to investigate the effect of nanogranular material on the rheological and frictional properties of faults. In this light, a re-visiting of the energy budget of faulting seems necessary to account for the interaction between various structures (present even along individual slip surfaces) and the work done to decrease the grain sizes to nanometers. Partitioning of energy between heat, grain breakage, intracrystalline deformation, amorphization, and seismic wave radiation will ultimately influence how much energy goes into heating (Bestmann et al., 2011; Knieke et al., 2011; Ranganathan et al., 2021; Rosakis et al., 2000; B. Wilson et al., 2005). Heating of fault zones and the associated microstructural changes present the best opportunity to

696 distinguish between fault segments that underwent rapid slip form fault segments that crept at slow
697 rates (Rowe & Griffith, 2015 and references therein).

698

699 **6 Acknowledgments**

700 Funding for the CORD technician support from NSF # 1833478 and funding by the J.H. and E.V.
701 Wade Fund from MIT's research support committee is gratefully acknowledged. We would also
702 like to acknowledge the staff at the Materials Research Science and Engineering Centers at the
703 Massachusetts Institute of Technology for their help with their ZEISS Merlin HR-SEM.

704 We would also like to thank Christie Rowe and McGill University, who allowed us to join their
705 2019 field course and collect the Waterman Hill samples. The MIT-EAPS 2020 field course for
706 allowing us to collect the Big Piute samples, and Juan Ignacio Arroyo Verástegui, who helped me
707 collect the sample from Falla de Plan de los Plátanos.

708

7 Appendix

The accuracy of the signal processing technique was assessed by recording the difference between the "input" Hurst exponents of randomly generated synthetic isotropic self-affine surfaces using the code provided in Candela et al. (2009) and the "output" recovered with our methods. For each value of the input Hurst exponent, we analyzed a set of 1000 synthetically generated surfaces as presented in Fig. A1. We further assessed our method by analyzing surface data from the Corona Heights fault surface samples from Thom et al. (2017). The average Hurst exponents of the Corona Heights Fault slickenside samples corresponded to 0.72 ±. 0.11 and 0.78 ± 0.09 for the parallel and perpendicular orientations, respectively. However, when the data in both directions are taken into account, we obtained 0.75 ± 0.10, which agrees with the value found by Thom et al. (2017).

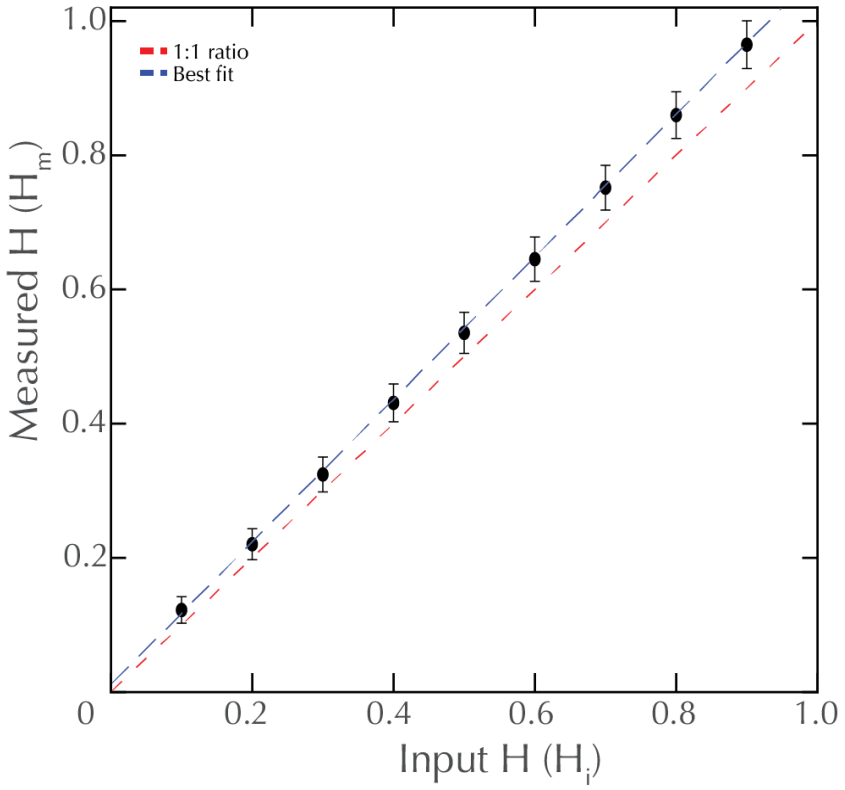

Figure A1. Calibration of PSD method for calculating the Hurst exponent (*H*). Note that the measured Hurst exponent (H_m) does not follow a one-to-one ratio (red). Instead, it has a linear best fit of the form $H_m = 1.065\ H_i + 0.006$ with a coefficient of determination R^2=0.999.

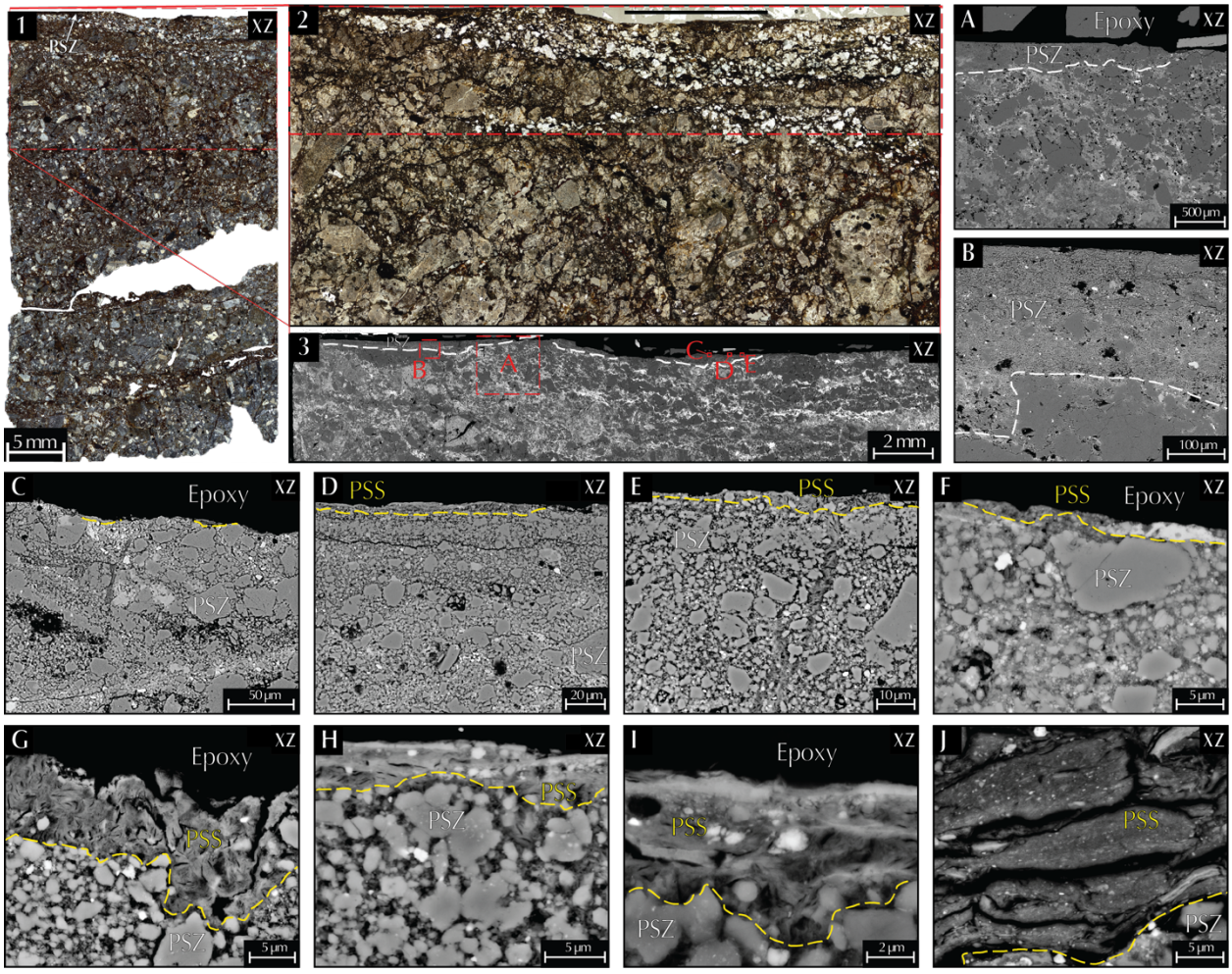

Figure A2. Set of images at progressively higher magnifications used in the GSD determination of andesite hosted slickenside. See text for details.

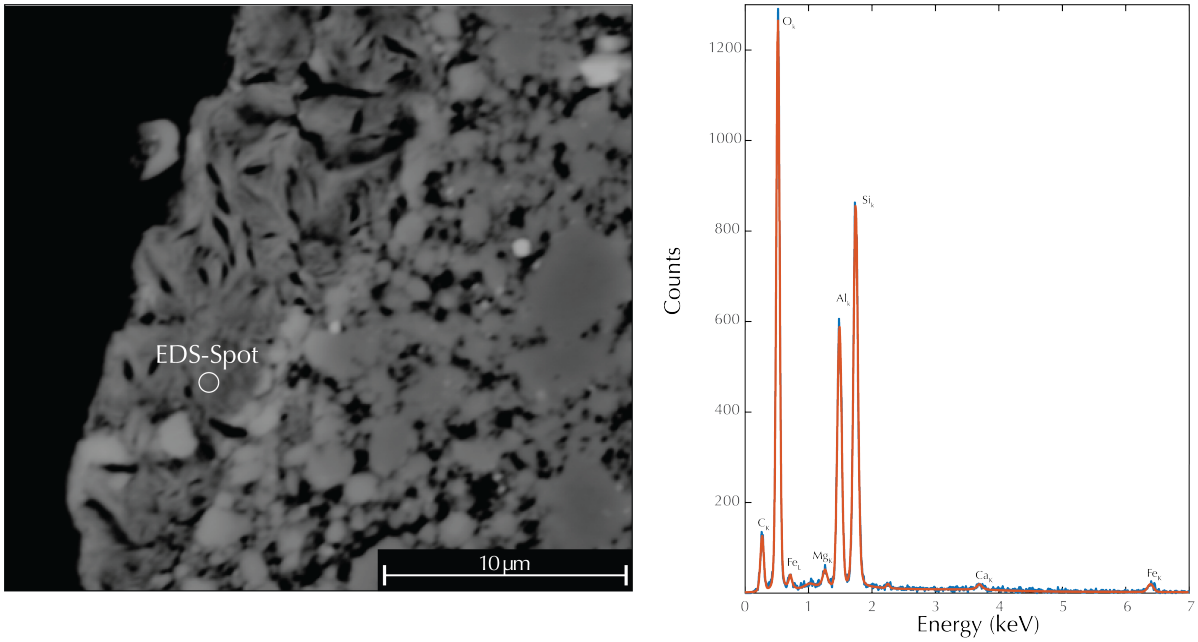

Figure A3. EDS-spectrum of "wispy" PSS from andesite hosted slickensides.

8 Data Availability Statement

Data reported here are publicly available at Zenodo Repository at: https://doi.org/10.5281/zenodo.6558132 (SEM and petrographic photomicrographs), https://doi.org/10.5281/zenodo.5167913 (surface roughness data), and https://doi.org/10.5281/zenodo.6558649 (grain size distribution data) under a Creative Commons Attribution 4.0 International Public License.

9 References

Ault, A. K., Jensen, J. L., McDermott, R. G., Shen, F.-A., & Van Devener, B. R. (2019). Nanoscale evidence for temperature-induced transient rheology and postseismic fault healing. *Geology*, *47*(12), 1203–1207. https://doi.org/10.1130/G46317.1

Ben-Nun, O., Einav, I., & Tordesillas, A. (2010). Force attractor in confined comminution of granular materials. *Physical Review Letters*, *104*(10), 108001.

https://doi.org/10.1103/PhysRevLett.104.108001

Ben-Zion, Y., & Rice, J. R. (1997). Dynamic simulations of slip on a smooth fault in an elastic solid. *Journal of Geophysical Research*, *102*(B8), 17771–17784. https://doi.org/10.1029/97jb01341

Berthé, D., Choukroune, P., & Jegouzo, P. (1979). Orthogneiss, mylonite and non coaxial deformation of granites: the example of the South Armorican Shear Zone. *Journal of Structural Geology*, *1*(1), 31–42. https://doi.org/10.1016/0191-8141(79)90019-1

Bestmann, M., Pennacchioni, G., Frank, G., Göken, M., & de Wall, H. (2011). Pseudotachylyte in muscovite-bearing quartzite: Coseismic friction-induced melting and plastic deformation of quartz. *Journal of Structural Geology*, *33*(2), 169–186. https://doi.org/10.1016/j.jsg.2010.10.009

Bhushan, B. (2013). *Introduction to Tribology*. John Wiley & Sons. Retrieved from https://play.google.com/store/books/details?id=b0nhJrqsoZ0C

Billi, A., & Storti, F. (2004). Fractal distribution of particle size in carbonate cataclastic rocks from the core of a regional strike-slip fault zone. *Tectonophysics*, *384*(1), 115–128. https://doi.org/10.1016/j.tecto.2004.03.015

Bistacchi, A., Griffith, W. A., Smith, S. A. F., Di Toro, G., Jones, R., & Nielsen, S. (2011). Fault Roughness at Seismogenic Depths from LIDAR and Photogrammetric Analysis. *Pure and Applied Geophysics*, *168*(12), 2345–2363. https://doi.org/10.1007/s00024-011-0301-7

Boneh, Y., & Reches, Z. (2018). Geotribology - Friction, wear, and lubrication of faults. *Tectonophysics*, *733*, 171–181. https://doi.org/10.1016/j.tecto.2017.11.022

Boneh, Y., Chang, J. C., Lockner, D. A., & Reches, Z. (2014). Evolution of Wear and Friction

Along Experimental Faults. *Pure and Applied Geophysics*, *171*(11), 3125–3141. https://doi.org/10.1007/s00024-014-0801-3

Bowden, F. P., Tabor, D., & Taylor, G. I. (1939). The area of contact between stationary and moving surfaces. *Proceedings of the Royal Society of London. Series A, Mathematical and Physical Sciences*, *169*(938), 391–413. https://doi.org/10.1098/rspa.1939.0005

Brodsky, E. E., Kirkpatrick, J. D., & Candela, T. (2016). Constraints from fault roughness on the scale-dependent strength of rocks. *Geology*, *44*(1), 19–22. https://doi.org/10.1130/G37206.1

Brodsky, E. E., McLaskey, G. C., & Ke, C.-Y. (2020). Groove generation and coalescence on a large-scale laboratory fault. *AGU Advances*, *1*(4). https://doi.org/10.1029/2020av000184

Brown, C. A., Hansen, H. N., Jiang, X. J., Blateyron, F., Berglund, J., Senin, N., et al. (2018). Multiscale analyses and characterizations of surface topographies. *CIRP Annals*, *67*(2), 839–862. https://doi.org/10.1016/j.cirp.2018.06.001

Brown, S. R., & Scholz, C. H. (1985). Broad bandwidth study of the topography of natural rock surfaces. *Journal of Geophysical Research*, *90*(B14), 12575. https://doi.org/10.1029/jb090ib14p12575

Bruhat, L., Klinger, Y., Vallage, A., & Dunham, E. M. (2020). Influence of fault roughness on surface displacement: from numerical simulations to coseismic slip distributions. *Geophysical Journal International*, *220*(3), 1857–1877. https://doi.org/10.1093/gji/ggz545

Caine, J. S., Evans, J. P., & Forster, C. B. (1996). Fault zone architecture and permeability structure. *Geology*, *24*(11), 1025–1028. https://doi.org/10.1130/0091-7613(1996)024<1025:FZAAPS>2.3.CO;2

791 Candela, T., Renard, F., Bouchon, M., Brouste, A., Marsan, D., Schmittbuhl, J., & Voisin, C.
792 (2009). Characterization of Fault Roughness at Various Scales: Implications of Three-
793 Dimensional High Resolution Topography Measurements. *Pure and Applied Geophysics*,
794 *166*(10), 1817–1851. https://doi.org/10.1007/s00024-009-0521-2
795 Candela, T., Renard, F., Klinger, Y., Mair, K., Schmittbuhl, J., & Brodsky, E. E. (2012).
796 Roughness of fault surfaces over nine decades of length scales. *Journal of Geophysical*
797 *Research*, *117*(B8). https://doi.org/10.1029/2011jb009041
798 Cattania, C., & Segall, P. (2021). Precursory slow slip and foreshocks on rough faults. *Journal of*
799 *Geophysical Research, [Solid Earth]*, *126*(4). https://doi.org/10.1029/2020jb020430
800 Chen, J., Verberne, B. A., & Niemeijer, A. R. (2020). Flow-to-Friction Transition in Simulated
801 Calcite Gouge: Experiments and Microphysical Modeling. *Journal of Geophysical*
802 *Research, [Solid Earth]*, *125*(11), e2020JB019970.
803 https://doi.org/10.1029/2020JB019970
804 Chen, X., Madden, A. S., Bickmore, B. R., & Reches, Z. (2013). Dynamic weakening by
805 nanoscale smoothing during high-velocity fault slip. *Geology*, *41*(7), 739–742.
806 https://doi.org/10.1130/G34169.1
807 Chester, F. M., & Logan, J. M. (1986). Implications for mechanical properties of brittle faults
808 from observations of the Punchbowl fault zone, California. *Pure and Applied Geophysics*,
809 *124*(1), 79–106. https://doi.org/10.1007/BF00875720
810 Chester, F. M., Friedman, M., & Logan, J. M. (1985). Foliated cataclasites. *Tectonophysics*,
811 *111*(1), 139–146. https://doi.org/10.1016/0040-1951(85)90071-X
812 Chester, F. M., Evans, J. P., & Biegel, R. L. (1993). Internal structure and weakening
813 mechanisms of the San Andreas Fault. *Journal of Geophysical Research*, *98*(B1), 771–

786. https://doi.org/10.1029/92jb01866

Chester, J. S., Chester, F. M., & Kronenberg, A. K. (2005). Fracture surface energy of the Punchbowl fault, San Andreas system. *Nature*, *437*(7055), 133–136. https://doi.org/10.1038/nature03942

Chu, S. X., Tsai, V. C., Trugman, D. T., & Hirth, G. (2021). Fault interactions enhance high-frequency earthquake radiation. *Geophysical Research Letters*, *48*(20). https://doi.org/10.1029/2021gl095271

Cox, S. J. D., & Scholz, C. H. (1988). On the formation and growth of faults: an experimental study. *Journal of Structural Geology*. Retrieved from https://www.sciencedirect.com/science/article/pii/0191814188900193

De la Teja Segura, M. Á., & Roque Ayala, A. (2007). Carta Geológica-Minera Autlán de Navarro E13-B12 Jalisco. (S. G. Mexicano, Ed.). Pachuca, HGO, Mexico : Servicio Geológico Mexicano. Retrieved from http://mapserver.sgm.gob.mx/Cartas_Online/geologia/956_E13-B12_GM.pdf

De Paola, N. (2013). Nano-powder coating can make fault surfaces smooth and shiny: implications for fault mechanics? *Geology*, *41*(6), 719–720. https://doi.org/10.1130/focus062013.1

Di Toro, G., Han, R., Hirose, T., De Paola, N., Nielsen, S., Mizoguchi, K., et al. (2011). Fault lubrication during earthquakes. *Nature*, *471*(7339), 494–498. https://doi.org/10.1038/nature09838

Dieterich, J. H., & Kilgore, B. D. (1996). Imaging surface contacts: power law contact distributions and contact stresses in quartz, calcite, glass and acrylic plastic. *Tectonophysics*, *256*(1), 219–239. https://doi.org/10.1016/0040-1951(95)00165-4

837 Doblas, M. (1998). Slickenside kinematic indicators. *Tectonophysics*, *295*(1), 187–197.
838 https://doi.org/10.1016/S0040-1951(98)00120-6
839 Dor, O., & Reches, Z. (2005). *Analysis of Fault Zones Associated with Large Earthquakes in*
840 *South African Gold Mines*. Earth Sciences Institute, Hebrew University, Jerusalem,
841 Israel. Retrieved from http://earthquakes.ou.edu/nelsam/fault_zones.pdf
842 Evans, J. P., Prante, M. R., Janecke, S. U., & Ault, A. K. (2014). Hot faults: Iridescent slip
843 surfaces with metallic luster document high-temperature ancient seismicity in the
844 Wasatch fault zone, Utah, USA. Retrieved from
845 https://pubs.geoscienceworld.org/gsa/geology/article-abstract/42/7/623/131640
846 Faulkner, D. R., Lewis, A. C., & Rutter, E. H. (2003). On the internal structure and mechanics of
847 large strike-slip fault zones: field observations of the Carboneras fault in southeastern
848 Spain. *Tectonophysics*, *367*(3), 235–251. https://doi.org/10.1016/S0040-1951(03)00134-3
849 Faulkner, D. R., Jackson, C. A. L., Lunn, R. J., Schlische, R. W., Shipton, Z. K., Wibberley, C.
850 A. J., & Withjack, M. O. (2010). A review of recent developments concerning the
851 structure, mechanics and fluid flow properties of fault zones. *Journal of Structural*
852 *Geology*, *32*(11), 1557–1575. https://doi.org/10.1016/j.jsg.2010.06.009
853 Faulkner, D. R., Mitchell, T. M., Jensen, E., & Cembrano, J. (2011). Scaling of fault damage
854 zones with displacement and the implications for fault growth processes. *Journal of*
855 *Geophysical Research*, *116*(B5). https://doi.org/10.1029/2010jb007788
856 Ferrari, L., Pasquaré, G., Venegas-Salgado, S., & Romero-Rios, F. (2000). Geology of the
857 western Mexican Volcanic Belt and adjacent Sierra Madre Occidental and Jalisco Block.
858 In *Cenozoic tectonics and volcanism of Mexico* (pp. 65–83). Geological Society of
859 America. https://doi.org/10.1130/0-8137-2334-5.65

Finch, M. A., Bons, P. D., Steinbach, F., Griera, A., Llorens, M.-G., Gomez-Rivas, E., et al. (2020). The ephemeral development of C′ shear bands: A numerical modelling approach. *Journal of Structural Geology*, *139*, 104091. https://doi.org/10.1016/j.jsg.2020.104091

Fletcher, J. M., & Karlstrom, K. E. (1990). Late Cretaceous ductile deformation, metamorphism and plutonism in the Piute Mountains, eastern Mojave Desert. *Journal of Geophysical Research*, *95*(B1), 487. https://doi.org/10.1029/jb095ib01p00487

Fletcher, J. M., Bendixen, J., Fillmore, R., Walker, J. D., Glazner, A. F., & Bartley, J. M. (1999). Geology of the Mitchel Range and Waterman Hills, San Bernardino County, California. Geological society of America. https://doi.org/10.1130/1999-fletcher-watermanhills

Fleuty, M. J. (1975). Slickensides and slickenlines. *Geological Magazine*, *112*(3), 319–322. https://doi.org/10.1017/S0016756800047087

Fondriest, M., Mecklenburgh, J., Passelegue, F. X., Artioli, G., Nestola, F., Spagnuolo, E., et al. (2020). Pseudotachylyte alteration and the rapid fade of earthquake scars from the geological record. *Geophysical Research Letters*, *47*(22). https://doi.org/10.1029/2020gl090020

Gadelmawla, E. S., Koura, M. M., Maksoud, T. M. A., Elewa, I. M., & Soliman, H. H. (2002). Roughness parameters. *Journal of Materials Processing Technology*, *123*(1), 133–145. https://doi.org/10.1016/S0924-0136(02)00060-2

Ghosh, A., & Sadeghi, F. (2015). A novel approach to model effects of surface roughness parameters on wear. *Wear: An International Journal on the Science and Technology of Friction Lubrication and Wear*, *338–339*, 73–94. https://doi.org/10.1016/j.wear.2015.04.022

Glazner, A. F., & Mills, R. D. (2012). Interpreting two-dimensional cuts through broken

geologic objects: Fractal and non-fractal size distributions. *Geosphere*, *8*(4), 902–914. https://doi.org/10.1130/GES00731.1

Glazner, A. F., Bartley, J. M., & Douglas Walker, J. (1989). Magnitude and significance of Miocene crustal extension in the central Mojave Desert, California. *Geology*, *17*(1), 50–53. https://doi.org/10.1130/0091-7613(1989)017<0050:MASOMC>2.3.CO;2

Gold, P. O., Behr, W. M., Fletcher, J. M., Rockwell, T. K., & Figueiredo, P. M. (2020). Time-invariant late Quaternary slip rates along the Agua Blanca fault, northern Baja California, Mexico. *Tectonics*, *39*(9). https://doi.org/10.1029/2019tc005788

Goldberg, R., Siman-Tov, S., & Emmanuel, S. (2016). Weathering resistance of carbonate fault mirrors promotes rupture localization. *Geophysical Research Letters*. https://doi.org/10.1002/2016gl067788

Graves, R., & Pitarka, A. (2016). Kinematic Ground-Motion Simulations on Rough Faults Including Effects of 3D Stochastic Velocity PerturbationsKinematic Ground-Motion Simulations on Rough Faults. *Bulletin of the Seismological Society of America*, *106*(5), 2136–2153. https://doi.org/10.1785/0120160088

Gu, C., Meng, X., Wang, S., & Ding, X. (2021). Study on the mutual influence of surface roughness and texture features of rough-textured surfaces on the tribological properties. *Proceedings of the Institution of Mechanical Engineers, Part J: Journal of Engineering Tribology*, *235*(2), 256–273. https://doi.org/10.1177/1350650120940211

Han, S., Zhao, L., Jiang, Q., & Lian, J. (2012). Deformation-induced localized solid-state amorphization in nanocrystalline nickel. *Scientific Reports*, *2*, 493. https://doi.org/10.1038/srep00493

Harbord, C. W. A., Nielsen, S. B., De Paola, N., & Holdsworth, R. E. (2017). Earthquake

nucleation on rough faults. *Geology*, *45*(10), 931–934. https://doi.org/10.1130/G39181.1

Heesakkers, V., Murphy, S., & Reches, Z. (2011). Earthquake Rupture at Focal Depth, Part I: Structure and Rupture of the Pretorius Fault, TauTona Mine, South Africa. *Pure and Applied Geophysics*, *168*(12), 2395–2425. https://doi.org/10.1007/s00024-011-0354-7

Heilbronner, R., & Barrett, S. (2014). Fractal Grain Size Distributions. In R. Heilbronner & S. Barrett (Eds.), *Image Analysis in Earth Sciences: Microstructures and Textures of Earth Materials* (pp. 225–249). Berlin, Heidelberg: Springer Berlin Heidelberg. https://doi.org/10.1007/978-3-642-10343-8_13

Hippertt, J. (1999). Are S–C structures, duplexes and conjugate shear zones different manifestations of the same scale-invariant phenomenon? *Journal of Structural Geology*, *21*(8), 975–984. https://doi.org/10.1016/S0191-8141(99)00047-4

Houser, L. M., Ault, A. K., Newell, D. L., Evans, J. P., Shen, F.-A., & Van Devener, B. R. (2021). Nanoscale textural and chemical evolution of silica fault mirrors in the Wasatch fault damage zone, Utah, USA. *Geochemistry, Geophysics, Geosystems*, *22*(3). https://doi.org/10.1029/2020gc009368

Jacobs, T. D. B., Junge, T., & Pastewka, L. (2017). Quantitative characterization of surface topography using spectral analysis. *Surface Topography: Metrology and Properties*, *5*(1), 013001. https://doi.org/10.1088/2051-672X/aa51f8

Jordan, P. G. (1987). The deformational behaviour of bimineralic limestone-halite aggregates. *Tectonophysics*, *135*(1), 185–197. https://doi.org/10.1016/0040-1951(87)90160-0

Kaneki, S., Oohashi, K., Hirono, T., & Noda, H. (2020). Mechanical amorphization of synthetic fault gouges during rotary-shear friction experiments at subseismic to seismic slip velocities. *Journal of Geophysical Research, [Solid Earth]*, *125*(10).

https://doi.org/10.1029/2020jb019956

Kearse, J., Kaneko, Y., Little, T., & Van Dissen, R. (2019). Curved slickenlines preserve direction of rupture propagation. *Geology*, *47*(9), 838–842. https://doi.org/10.1130/G46563.1

Keulen, N., Heilbronner, R., Stünitz, H., Boullier, A.-M., & Ito, H. (2007). Grain size distributions of fault rocks: A comparison between experimentally and naturally deformed granitoids. *Journal of Structural Geology*, *29*(8), 1282–1300. https://doi.org/10.1016/j.jsg.2007.04.003

Keulen, N., Stünitz, H., & Heilbronner, R. (2008). Healing microstructures of experimental and natural fault gouge. *Journal of Geophysical Research*, *113*(B6). https://doi.org/10.1029/2007jb005039

Kim, T. W., Bhushan, B., & Cho, Y. J. (2006). The contact behavior of elastic/plastic non-Gaussian rough surfaces. *Tribology Letters*, *22*(1), 1. https://doi.org/10.1007/s11249-006-9036-5

Kirkpatrick, J. D., & Brodsky, E. E. (2014). Slickenline orientations as a record of fault rock rheology. *Earth and Planetary Science Letters*, *408*, 24–34. https://doi.org/10.1016/j.epsl.2014.09.040

Kirkpatrick, J. D., Rowe, C. D., White, J. C., & Brodsky, E. E. (2013). Silica gel formation during fault slip: Evidence from the rock record. *Geology*, *41*(9), 1015–1018. https://doi.org/10.1130/G34483.1

Knieke, C. (2012). *Fracture at the Nanoscale and the Limit of Grinding: Partikelbruch Im Nanometerbereich und Die Grenze Der Echtzerkleinerung*. Cuvillier.

Knieke, C., Romeis, S., & Peukert, W. (2011). Influence of process parameters on breakage

kinetics and grinding limit at the nanoscale. *AIChE Journal. American Institute of Chemical Engineers*, *57*(7), 1751–1758. https://doi.org/10.1002/aic.12408

Kotwal, C. A., & Bhushan, B. (1996). Contact Analysis of Non-Gaussian Surfaces for Minimum Static and Kinetic Friction and Wear. *Tribology Transactions*, *39*(4), 890–898. https://doi.org/10.1080/10402009608983609

Kuo, L.-W., Song, S.-R., Suppe, J., & Yeh, E.-C. (2016). Fault mirrors in seismically active fault zones: A fossil of small earthquakes at shallow depths. *Geophysical Research Letters*, *43*(5), 1950–1959. https://doi.org/10.1002/2015gl066882

Lee, J.-J., & Bruhn, R. L. (1996). Structural anisotropy of normal fault surfaces. *Journal of Structural Geology*, *18*(8), 1043–1059. https://doi.org/10.1016/0191-8141(96)00022-3

Lee, Y.-J. (1991). *Slickenside Petrography: slip-Sense Indicators and Classification* (Master of Sciences). (W. Means, Ed.). State University of New York at Albany. Retrieved from http://www.atmos.albany.edu/geology/theses/leeyjmstxt.pdf

Lin, A. (2001). S–C fabrics developed in cataclastic rocks from the Nojima fault zone, Japan and their implications for tectonic history. *Journal of Structural Geology*, *23*(6), 1167–1178. https://doi.org/10.1016/S0191-8141(00)00171-1

Lin, S., & Williams, P. F. (1992). The origin of ridge-in-groove slickenside striae and associated steps in an S-C mylonite. *Journal of Structural Geology*, *14*(3), 315–321. https://doi.org/10.1016/0191-8141(92)90089-F

Lin, S., Jiang, D., & Williams, P. F. (2007). Importance of differentiating ductile slickenside striations from stretching lineations and variation of shear direction across a high-strain zone. *Journal of Structural Geology*, *29*(5), 850–862. https://doi.org/10.1016/j.jsg.2006.12.006

975 Lyell, S. C. (Ed.). (1871). Chapter XXXVI. Mineral Veins. In *The student's elements of geology.*
976 (pp. 589–602). Thomas Telford Publishing. https://doi.org/10.1680/tseog.52581.0036
977 Macklin, C., Kaneko, Y., & Kearse, J. (2021). Coseismic slickenlines record the emergence of
978 multiple rupture fronts during a surface-breaking earthquake. *Tectonophysics*, *808*,
979 228834. https://doi.org/10.1016/j.tecto.2021.228834
980 Magloughlin, J. F., & Spray, J. G. (1992). Frictional melting processes and products in
981 geological materials: introduction and discussion. *Tectonophysics*, *204*(3), 197–204.
982 https://doi.org/10.1016/0040-1951(92)90307-R
983 Mandelbrot, B. B. (1985). Self-Affine Fractals and Fractal Dimension. *Physica Scripta*, *32*(4),
984 257. https://doi.org/10.1088/0031-8949/32/4/001
985 Marti, S., Stünitz, H., Heilbronner, R., & Plümper, O. (2020). Amorphous material in
986 experimentally deformed mafic rock and its temperature dependence: Implications for
987 fault rheology during aseismic creep and seismic rupture. *Journal of Structural Geology*,
988 *138*, 104081. https://doi.org/10.1016/j.jsg.2020.104081
989 McCool, J. I. (1992). Non-Gaussian effects in microcontact. *International Journal of Machine*
990 *Tools & Manufacture*, *32*(1), 115–123. https://doi.org/10.1016/0890-6955(92)90068-R
991 Milanese, E., Brink, T., Aghababaei, R., & Molinari, J.-F. (2019). Emergence of self-affine
992 surfaces during adhesive wear. *Nature Communications*, *10*(1), 1116.
993 https://doi.org/10.1038/s41467-019-09127-8
994 Nakamura, N., & Nagahama, H. (2002). Tribochemical wearing in S-C mylonites and its
995 implication to lithosphere stress level. *Earth, Planets and Space*, *54*(11), 1103–1108.
996 https://doi.org/10.1186/bf03353309
997 Nielsen, S., Mosca, P., Giberti, G., Di Toro, G., Hirose, T., & Shimamoto, T. (2010). On the

transient behavior of frictional melt during seismic slip. *Journal of Geophysical Research*, *115*(B10). https://doi.org/10.1029/2009jb007020

Ohl, M., Plümper, O., Chatzaras, V., Wallis, D., Vollmer, C., & Drury, M. (2020). Mechanisms of fault mirror formation and fault healing in carbonate rocks. *Earth and Planetary Science Letters*, *530*, 115886. https://doi.org/10.1016/j.epsl.2019.115886

Ortega-Arroyo, D. (2017). *The Rock Record of Seismic Nucleation and Dynamic Weakening: Case Studies from the Whipple Mountains Detachment Fault, Eastern California*. University of Texas at Austin.

Otsubo, M., Shigematsu, N., Imanishi, K., Ando, R., Takahashi, M., & Azuma, T. (2013). Temporal slip change based on curved slickenlines on fault scarps along Itozawa fault caused by 2011 Iwaki earthquake, northeast Japan. *Tectonophysics*, *608*, 970–979. https://doi.org/10.1016/j.tecto.2013.07.022

Passchier, C. W., & Trouw, R. A. J. (2005). *Microtectonics*. Springer, Berlin, Heidelberg. https://doi.org/10.1007/3-540-29359-0

Pec, M., & Al Nasser, S. (2021). Formation of nanocrystalline and amorphous materials causes parallel brittle-viscous flow of crustal rocks: Experiments on quartz-feldspar aggregates. *Journal of Geophysical Research, [Solid Earth]*, *126*(5). https://doi.org/10.1029/2020jb021262

Pec, M., Stünitz, H., Heilbronner, R., Drury, M., & de Capitani, C. (2012). Origin of pseudotachylites in slow creep experiments. *Earth and Planetary Science Letters*, *355–356*, 299–310. https://doi.org/10.1016/j.epsl.2012.09.004

Pec, M., Stünitz, H., Heilbronner, R., & Drury, M. (2016). Semi-brittle flow of granitoid fault rocks in experiments. *Journal of Geophysical Research, [Solid Earth]*, *121*(3), 1677–

1705. https://doi.org/10.1002/2015jb012513

Petit, J. P. (1987). Criteria for the sense of movement on fault surfaces in brittle rocks. *Journal of Structural Geology*, *9*(5), 597–608. https://doi.org/10.1016/0191-8141(87)90145-3

Power, W. L., & Tullis, T. E. (1989). The relationship between slickenside surfaces in fine-grained quartz and the seismic cycle. *Journal of Structural Geology*, *11*(7), 879–893. https://doi.org/10.1016/0191-8141(89)90105-3

Power, W. L., Tullis, T. E., Brown, S. R., Boitnott, G. N., & Scholz, C. H. (1987). Roughness of natural fault surfaces. *Geophysical Research Letters*, *14*(1), 29–32. https://doi.org/10.1029/gl014i001p00029

Ranganathan, M., Minchew, B., Meyer, C. R., & Pec, M. (2021, July 29). *Deformational-energy partitioning in glacier shear zones*. *Earth and Space Science Open Archive*. Earth and Space Science Open Archive. https://doi.org/10.1002/essoar.10507633.1

Renard, F., Mair, K., & Gundersen, O. (2012). Surface roughness evolution on experimentally simulated faults. *Journal of Structural Geology*, *45*, 101–112. https://doi.org/10.1016/j.jsg.2012.03.009

Romeis, S., Schmidt, J., & Peukert, W. (2016). Mechanochemical aspects in wet stirred media milling. *International Journal of Mineral Processing*, *156*, 24–31. https://doi.org/10.1016/j.minpro.2016.05.018

Rosakis, P., Rosakis, A. J., Ravichandran, G., & Hodowany, J. (2000). A thermodynamic internal variable model for the partition of plastic work into heat and stored energy in metals. *Journal of the Mechanics and Physics of Solids*, *48*(3), 581–607. https://doi.org/10.1016/S0022-5096(99)00048-4

Rosas-Elguera, J., Ferrari, L., Garduño-Monroy, V. H., & Urrutia-Fucugauchi, J. (1996).

Continental boundaries of the Jalisco block and their influence in the Pliocene-Quaternary kinematics of western Mexico. *Geology*, *24*(10), 921–924. https://doi.org/10.1130/0091-7613(1996)024<0921:CBOTJB>2.3.CO;2

Rowe, C. D., & Griffith, W. A. (2015). Do faults preserve a record of seismic slip: A second opinion. *Journal of Structural Geology*, *78*, 1–26. https://doi.org/10.1016/j.jsg.2015.06.006

Rowe, C. D., Ross, C., Swanson, M. T., Pollock, S., Backeberg, N. R., Barshi, N. A., et al. (2018). Geometric complexity of earthquake rupture surfaces preserved in pseudotachylyte networks. *Journal of Geophysical Research, [Solid Earth]*, *123*(9), 7998–8015. https://doi.org/10.1029/2018jb016192

Rowe, C. D., Lamothe, K., Rempe, M., Andrews, M., Mitchell, T. M., Di Toro, G., et al. (2019). Earthquake lubrication and healing explained by amorphous nanosilica. *Nature Communications*, *10*(1), 320. https://doi.org/10.1038/s41467-018-08238-y

Sagy, A., & Lyakhovsky, V. (2019). Stress patterns and failure around rough interlocked fault surface. *Journal of Geophysical Research, [Solid Earth]*, *124*(7), 7138–7154. https://doi.org/10.1029/2018jb017006

Sagy, A., Brodsky, E. E., & Axen, G. J. (2007). Evolution of fault-surface roughness with slip. *Geology*, *35*(3), 283–286. https://doi.org/10.1130/G23235A.1

Scholz, C. H. (2019). *The Mechanics of Earthquakes and Faulting* (3rd ed.). Cambridge: Cambridge University Press. https://doi.org/10.1017/9781316681473

Sedlaček, M., Podgornik, B., & Vižintin, J. (2012). Correlation between standard roughness parameters skewness and kurtosis and tribological behaviour of contact surfaces. *Tribology International*, *48*, 102–112. https://doi.org/10.1016/j.triboint.2011.11.008

Shervais, K. A. H., & Kirkpatrick, J. D. (2016). Smoothing and re-roughening processes: The geometric evolution of a single fault zone. *Journal of Structural Geology*, *91*, 130–143. https://doi.org/10.1016/j.jsg.2016.09.004

Siman-Tov, S., Aharonov, E., Sagy, A., & Emmanuel, S. (2013). Nanograins form carbonate fault mirrors. *Geology*, *41*(6), 703–706. https://doi.org/10.1130/G34087.1

Siman-Tov, S., Aharonov, E., Boneh, Y., & Reches, Z. (2015). Fault mirrors along carbonate faults: Formation and destruction during shear experiments. *Earth and Planetary Science Letters*, *430*, 367–376. https://doi.org/10.1016/j.epsl.2015.08.031

Spray, J. G. (1989). Slickenside formation by surface melting during the mechanical excavation of rock. *Journal of Structural Geology*, *11*(7), 895–905. https://doi.org/10.1016/0191-8141(89)90106-5

Spray, J. G. (1992). A physical basis for the frictional melting of some rock-forming minerals. *Tectonophysics*, *204*(3), 205–221. https://doi.org/10.1016/0040-1951(92)90308-S

Sun, H., & Pec, M. (2021). Nanometric flow and earthquake instability. *Nature Communications*, *12*(1), 6779. https://doi.org/10.1038/s41467-021-26996-0

Swanson, M. T. (1988). Pseudotachylyte-bearing strike-slip duplex structures in the Fort Foster Brittle Zone, S. Maine. *Journal of Structural Geology*, *10*(8), 813–828. https://doi.org/10.1016/0191-8141(88)90097-1

Tal, Y., Goebel, T., & Avouac, J.-P. (2020). Experimental and modeling study of the effect of fault roughness on dynamic frictional sliding. *Earth and Planetary Science Letters*, *536*(116133), 116133. https://doi.org/10.1016/j.epsl.2020.116133

Tayebi, N., & Polycarpou, A. A. (2004). Modeling the effect of skewness and kurtosis on the static friction coefficient of rough surfaces. *Tribology International*, *37*(6), 491–505.

https://doi.org/10.1016/j.triboint.2003.11.010

Taylor, M. P., Ault, A. K., Odlum, M. L., & Newell, D. L. (2021). Shallow rupture propagation of Pleistocene earthquakes along the hurricane fault, UT, revealed by hematite (U-Th)/he thermochronometry and textures. *Geophysical Research Letters*, *48*(17). https://doi.org/10.1029/2021gl094379

Thom, C. A., Brodsky, E. E., Carpick, R. W., Pharr, G. M., Oliver, W. C., & Goldsby, D. L. (2017). Nanoscale roughness of natural fault surfaces controlled by scale-dependent yield strength. *Geophysical Research Letters*, *44*(18), 9299–9307. https://doi.org/10.1002/2017gl074663

Tikoff, B., Chatzaras, V., Newman, J., & Roberts, N. M. (2019). Big data in microstructure analysis: Building a universal orientation system for thin sections. *Journal of Structural Geology*, *125*, 226–234. https://doi.org/10.1016/j.jsg.2018.09.019

Tisato, N., Di Toro, G., De Rossi, N., Quaresimin, M., & Candela, T. (2012). Experimental investigation of flash weakening in limestone. *Journal of Structural Geology*, *38*, 183–199. https://doi.org/10.1016/j.jsg.2011.11.017

Tomota, T., Kondoh, Y., & Ohmori, T. (2019). Modeling Solid Contact between Smooth and Rough Surfaces with Non-Gaussian Distributions. *Tribology Transactions*, *62*(4), 580–591. https://doi.org/10.1080/10402004.2019.1573341

Torabi, A., Ellingsen, T. S. S., Johannessen, M. U., Alaei, B., Rotevatn, A., & Chiarella, D. (2020). Fault zone architecture and its scaling laws: where does the damage zone start and stop? *Geological Society, London, Special Publications*, *496*(1), 99–124. https://doi.org/10.1144/SP496-2018-151

Torabi, A., Balsamo, F., Nogueira, F. C. C., Vasconcelos, D. L., Silva, A. C. E., Bezerra, F. H.

R., & Souza, J. A. B. (2021). Variation of thickness, internal structure and petrophysical properties in a deformation band fault zone in siliciclastic rocks. *Marine and Petroleum Geology*, *133*, 105297. https://doi.org/10.1016/j.marpetgeo.2021.105297

Toy, V. G., Niemeijer, A., Renard, F., Morales, L., & Wirth, R. (2017). Striation and slickenline development on quartz fault surfaces at crustal conditions: Origin and effect on friction. *Journal of Geophysical Research, [Solid Earth]*, *122*(5), 3497–3512. https://doi.org/10.1002/2016jb013498

Tsai, V. C., & Hirth, G. (2020). Elastic impact consequences for high-frequency earthquake ground motion. *Geophysical Research Letters*, *47*(5). https://doi.org/10.1029/2019gl086302

Tsai, V. C., Hirth, G., Trugman, D. T., & Chu, S. X. (2021). Impact versus frictional earthquake models for high-frequency radiation in complex fault zones. *Journal of Geophysical Research, [Solid Earth]*, *126*(8). https://doi.org/10.1029/2021jb022313

Ulrich, T., Gabriel, A.-A., Ampuero, J.-P., & Xu, W. (2019). Dynamic viability of the 2016 Mw 7.8 Kaikōura earthquake cascade on weak crustal faults. *Nature Communications*, *10*(1), 1213. https://doi.org/10.1038/s41467-019-09125-w

Verberne, B. A., Plümper, O., de Winter, D. A. M., & Spiers, C. J. (2014). Rock mechanics. Superplastic nanofibrous slip zones control seismogenic fault friction. *Science*, *346*(6215), 1342–1344. https://doi.org/10.1126/science.1259003

Verberne, B. A., Plümper, O., & Spiers, C. J. (2019). Nanocrystalline Principal Slip Zones and Their Role in Controlling Crustal Fault Rheology. *Minerals*, *9*(6), 328. https://doi.org/10.3390/min9060328

Viat, A., Guillonneau, G., Fouvry, S., Kermouche, G., Sao Joao, S., Wehrs, J., et al. (2017).

Brittle to ductile transition of tribomaterial in relation to wear response at high temperatures. *Wear: An International Journal on the Science and Technology of Friction Lubrication and Wear*, *392–393*, 60–68. https://doi.org/10.1016/j.wear.2017.09.015

Viti, C., Brogi, A., Liotta, D., Mugnaioli, E., Spiess, R., Dini, A., et al. (2016). Seismic slip recorded in tourmaline fault mirrors from Elba Island (Italy). *Journal of Structural Geology*, *86*, 1–12. https://doi.org/10.1016/j.jsg.2016.02.013

Wang, M., Chen, Y.-F., Ma, G.-W., Zhou, J.-Q., & Zhou, C.-B. (2016). Influence of surface roughness on nonlinear flow behaviors in 3D self-affine rough fractures: Lattice Boltzmann simulations. *Advances in Water Resources*, *96*, 373–388. https://doi.org/10.1016/j.advwatres.2016.08.006

Wang, W.-Z., Chen, H., Hu, Y.-Z., & Wang, H. (2006). Effect of surface roughness parameters on mixed lubrication characteristics. *Tribology International*, *39*(6), 522–527. https://doi.org/10.1016/j.triboint.2005.03.018

Will, T. M., & Wilson, C. J. L. (1989). Experimentally produced slickenside lineations in pyrophyllitic clay. *Journal of Structural Geology*, *11*(6), 657–667. https://doi.org/10.1016/0191-8141(89)90002-3

Wilson, B., Dewers, T., Reches, Z., & Brune, J. (2005). Particle size and energetics of gouge from earthquake rupture zones. *Nature*, *434*(7034), 749–752. https://doi.org/10.1038/nature03433

Wilson, C. J. L., & Will, T. M. (1990). Slickenside lineations due to ductile processes. *Geological Society, London, Special Publications*, *54*(1), 455–460. https://doi.org/10.1144/GSL.SP.1990.054.01.41

Yan, X.-L., Wang, X.-L., & Zhang, Y.-Y. (2014). Influence of Roughness Parameters Skewness

and Kurtosis on Fatigue Life Under Mixed Elastohydrodynamic Lubrication Point Contacts. *Journal of Tribology*, *136*(3). https://doi.org/10.1115/1.4027480

Zhang, S., Wang, W., & Zhao, Z. (2014). The effect of surface roughness characteristics on the elastic–plastic contact performance. *Tribology International*, *79*, 59–73. https://doi.org/10.1016/j.triboint.2014.05.016

Zhang, Y. S., Zhang, L. C., Niu, H. Z., Bai, X. F., Yu, S., Ma, X. Q., & Yu, Z. T. (2014). Deformation twinning and localized amorphization in nanocrystalline tantalum induced by sliding friction. *Materials Letters*, *127*, 4–7. https://doi.org/10.1016/j.matlet.2014.04.079

Zhao, S., Hahn, E. N., Kad, B., Remington, B. A., Wehrenberg, C. E., Bringa, E. M., & Meyers, M. A. (2016). Amorphization and nanocrystallization of silicon under shock compression. *Acta Materialia*, *103*, 519–533. https://doi.org/10.1016/j.actamat.2015.09.022